Advances in Water Resources 122 (2018) 70–84

Contents lists available at ScienceDirect

Advances in Water Resources

journal homepage: www.elsevier.com/locate/advwatres

Image-based micro-continuum model for gas flow in organic-rich shale rock

Bo Guo [a,1,*], Lin Ma [b,c], Hamdi A. Tchelepi [a]

[a] Department of Energy Resources Engineering, Stanford University, Stanford, CA, USA
[b] School of Earth, Atmospheric, and Environmental Sciences, University of Manchester, Manchester, UK
[c] Manchester X-ray Imaging Facility, School of Materials, University of Manchester, Manchester, UK

ARTICLE INFO

Keywords:
Shale gas
Nanoporous media
Micro-continuum
Darcy–Brinkman–Stokes

ABSTRACT

The physical mechanisms that control the flow dynamics in organic-rich shale are not well understood. The challenges include nanometer-scale pores and multiscale heterogeneity in the spatial distribution of the constituents. Recently, digital rock physics (DRP), which uses high-resolution images of rock samples as input for flow simulations, has been used for shale. One important issue with images of shale rock is sub-resolution porosity (nanometer pores below the instrument resolution), which poses serious challenges for instruments and computational models. Here, we present a micro-continuum model based on the Darcy–Brinkman–Stokes framework. The method couples resolved pores and unresolved nano-porous regions using physics-based parameters that can be measured independently. The Stokes equation is used for resolved pores. The unresolved nano-porous regions are treated as a continuum, and a permeability model that accounts for slip-flow and Knudsen diffusion is employed. Adsorption/desorption and surface diffusion in organic matter are also accounted for. We apply our model to simulate gas flow in a high-resolution 3D segmented image of shale. The results indicate that the overall permeability of the sample (at fixed pressure) depends on the time scale. Early-time permeability is controlled by Stokes flow, while the late-time permeability is controlled by non-Darcy effects and surface-diffusion.

1. Introduction

Oil and gas production from unconventional subsurface resources, such as ultra-tight organic-rich shales, has increased significantly in the past decade. Shale gas now accounts for more than half of the gas production in the United States (EIA, 2017). Despite the rapid development of the shale gas industry, it remains challenging to predict and further enhance gas production from shale formations. The majority of gas in a shale formation is stored in the rock matrix - primarily in organic matter (Ross and Bustin, 2009; Gensterblum et al., 2015). During production, the stored gas has to travel through the matrix to reach natural and hydraulic fractures that provide pathways to the production well. Gas transport in the shale matrix is therefore one of the most critical processes for production. Understanding gas transport is also critical when considering using the depleted shale gas reservoir for carbon dioxide storage (Edwards et al., 2015). However, due to the complex pore structure and heterogeneity of the shale materials, gas transport mechanisms in the shale matrix are not well understood.

The shale rock matrix is strongly heterogeneous at multiple length scales in terms of pore structures and the material constituents, both of which may dictate gas transport in shale. The range of pore sizes in shale can be assessed using indirect petrophysical methods (Sondergeld et al., 2010; Chalmers et al., 2012; Clarkson et al., 2013), such as mercury injection capillary pressure (MICP), low pressure nitrogen adsorption, and nuclear magnetic resonance (NMR) spectroscopy. The measurements suggest that the majority of the pore sizes of shale are on the order of a few to tens of nanometers. In addition to the indirect measurements, several imaging techniques have been used to directly characterize shale samples in three dimensions (3D), such as X-ray computed tomography (e.g., micro-CT, nano-CT), focused ion beam scanning electron microscopy (FIB-SEM), helium ion microscopy (HIM), and transmission electron microscopy (TEM) tomography. Image characterizations often aim to understand the type, geometry, size, surface area, and connectivity of the pores, the distribution of material constituents, as well as the relationships between pores and constituents (Chalmers et al., 2012; Curtis et al., 2012; Ma et al., 2017). 3D shale images confirm the nanometer range of pores in shale inferred from indirect methods (Curtis et al., 2012). Kelly et al. (2016) assessed the utility of shale FIB-SEM images and concluded that FIB-SEM images may not provide a representative elementary volume (REV) for shale permeability. Limited by a trade-off between the image resolution and the field of view, multiple imaging techniques with different inherent resolutions may need to be combined to characterize larger shale samples (Ma et al., 2016; 2018; Wu et al., 2017). Wu et al. (2017) used micro-CT,

* Corresponding author.Present Address: Department of Hydrology and Atmospheric Sciences, University of Arizona, United States.
E-mail address: boguo@email.arizona.edu (B. Guo).
[1] Present Address: Department of Hydrology and Atmospheric Sciences, University of Arizona, Tucson, AZ, USA.

https://doi.org/10.1016/j.advwatres.2018.10.004
Received 25 July 2018; Received in revised form 21 September 2018; Accepted 3 October 2018
Available online 6 October 2018

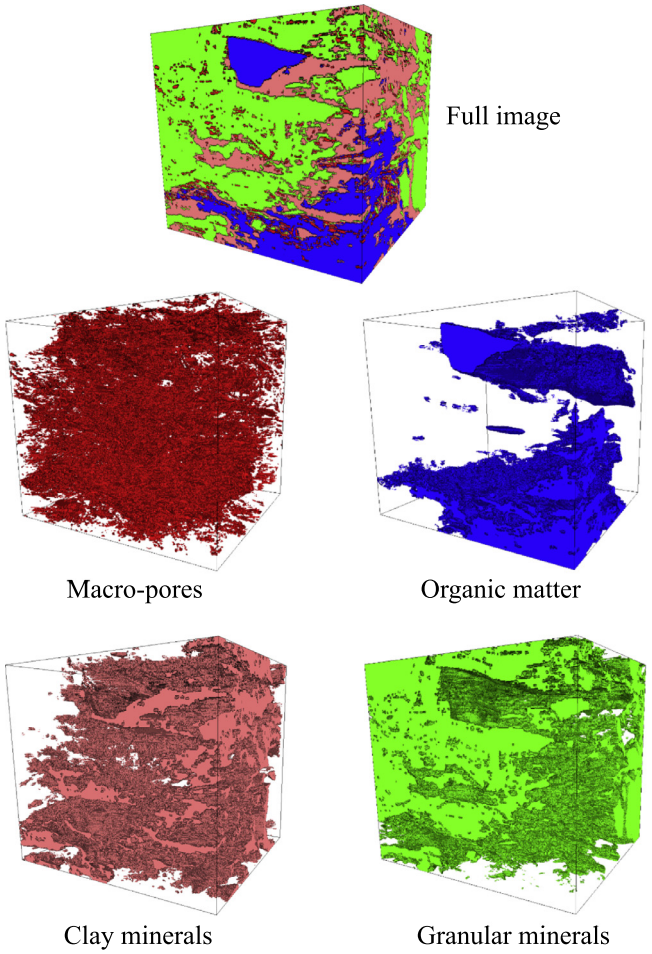

Fig. 1. 3D shale image reconstructed from FIB-SEM (Ma et al., 2018). The size of the image is: 7.22 μm × 5.11 μm × 6.82 μm; voxel size: 10 nm × 10 nm × 20 nm. Four material constituents are segmented: red - macro-pores; blue - organic matter; pink - clay minerals; green - granular minerals. The shale sample is from a core in the Haynesville–Bossier shale formation.(For interpretation of the references to color in this figure legend, the reader is referred to the web version of this article.)

nano-CT, FIB-SEM, and HIM to characterize a shale sample of 1.3^3 cm^3 and subsamples down to 3.25^3 μm^3. The highest resolution images obtained using HIM indicate that pores, which appeared to be isolated in lower resolution FIB-SEM images, are connected by smaller pores. Ma et al. (2016) and Ma et al. (2018) used micro-CT, nano-CT, and FIB-SEM to address the issue of an REV for porosity and different material constituents. Their highest resolution FIB-SEM images were segmented into four material constituents: macro-pores, organic matter, clay minerals, and granular minerals. We note that pores are commonly categorized as micropores (<2 nm), mesopores (2–50 nm), and macropores (>50 nm) (Rouquerol et al., 1994). Here, we use a different nomenclature and refer to the pores that are resolved in the image as macro-pores and pores that are below the image resolution as sub-resolution pores. Fig. 1 shows an example of a 3D FIB-SEM image from Ma et al. (2018) for a shale sample from the Haynesville–Bossier shale formation. The 3D digital images show the complexity of the pore space of shale. The image in Fig. 1 is used in our pore-scale simulation study (more details of the image are presented in Section 4).

The nanometer-range pores in shale rock lead to many interesting physical processes that deviate from the standard Darcy's law for flow in porous media, or the standard formulation of the Navier–Stokes equations at the pore-scale. This dates back to the work of Klinkenberg (1941) who reported that gas permeability of low permeable tight rocks is larger than their intrinsic permeability (e.g., measured with liquids), especially at low gas pressure. The Klinkenberg effect can be attributed to a non-zero slip velocity at the pore wall. Gas flow in small confined pores belongs to the subject of rarefied gas dynamics. Small confined pores lead to gas rarefaction where collisions between pore wall and gas molecules become important relative to the collisions between gas molecules. The extent of the rarefaction effect can be characterized by the Knudsen number (Kn), which is defined as the ratio between the mean free path to the characteristic geometric length of the flow conduit. Gas flow can be classified into four regimes (Karniadakis et al., 2005): continuum flow ($\mathrm{Kn} \lesssim 0.001$) where Navier–Stokes equations are applicable; slip flow ($0.001 < \mathrm{Kn} \lesssim 0.1$) in which the Navier–Stokes equations can still be applied, but with appropriate velocity slip conditions at the solid surface; transition flow ($0.1 < \mathrm{Kn} \lesssim 10$) where gas flow transits from slip flow to free molecular flow; free molecular flow ($\mathrm{Kn} > 10$) where the continuum-based Navier–Stokes equations are not applicable. Note that this classification is based on gas flow through an infinite channel with the thickness being the characteristic length. The regime boundaries (in terms of Kn) depend on the specific geometries of the conduits. Beskok and Karniadakis (1999) developed a unified model for rarefied gas flow in micro-channels, ducts, and pipes. Their model is applicable for all flow regimes ($0 \leq \mathrm{Kn} < \infty$). We refer to the unified model as the BK model. Wu and Zhang (2016) extended the BK model to include the effects of adsorption in the nano-channel accounting for migration of the adsorbed phase. Civan (2010) used the BK model to develop an apparent permeability for tight rocks using the bundle-of-tubes model, which was further extended to include surface diffusion (Xiong et al., 2012). Lunati and Lee (2014) developed a bundle-of-dual-tubes model for gas production from fractured shale formations. In the spirit of the dusty-gas model (Mason and Malinauskas, 1983), another group of apparent permeability models has been derived by a linear, or weighted, summation of the flux contributions from viscous flow, Knudsen diffusion, and surface diffusion (see Javadpour, 2009; Darabi et al., 2012; Sakhaee-Pour and Bryant, 2012; Wu et al., 2016). Landry et al. (2016) compared the BK model, the dusty-gas model, and the Javadpour (2009) model with the linearized Boltzmann solution for a straight tube. They reported that both the dusty-gas and the Javadpour (2009) models overestimate the permeability, while the BK model matches well with the linearized Boltzmann solution. In addition, Landry et al. (2016) showed that the bundle-of-tubes model can significantly overestimate the apparent permeability due to flow dependence on the pore shapes and connectivity in the slip and early-transition flow regimes. To date, the apparent permeability models in the literature are either limited to idealized porous media (i.e., bundle-of-tubes with correction for tortuosity) or composite porous media with a presumed distribution of constituents that allow for upscaling (Darabi et al., 2012; Akkutlu et al., 2015). The appropriate "apparent" permeability and other transport properties of shale rocks remain open questions.

Images of shale samples provide an opportunity to model the complex transport dynamics directly for natural shale samples. This should provide insight into the complex physics associated with transport in natural shales. The use of pore-scale imaging and numerical flow modeling, referred to as digital rock physics or analysis, is increasing for reservoir rocks (Blunt et al., 2013; Blunt, 2017). For unconventional source rocks (i.e., organic-rich shale), image-based pore-scale modeling is still in its infancy. Lattice Boltzmann methods (LBM), as a popular method for pore-scale simulation, has been used for direct numerical simulation of shale gas transport (Wang et al., 2016). Various studies have extended LBM to include the transport physics relevant to shale, e.g., Knudsen diffusion, slip flow, adsorption/desorption and surface diffusion (e.g., Chen et al., 2015; Wang et al., 2017). Another approach is to solve the Navier–Stokes equations in the pore structures using finite-volume discretization schemes. Because most of the pores are in the nanometer range, the applicability of the standard Navier–Stokes equations may be questioned. In addition, many pores with sizes in the nanometer range

cannot be resolved due to the limitation of image resolution. These sub-resolution pores are critical for gas transport as the important nanoscale physics (e.g., slip flow, Knudsen diffusion, adsorption/desorption, and surface diffusion) primarily take place in those unresolved nano-porous regions. Therefore, it is crucial to consider the sub-resolution pores and include the nanoscale transport physics.

For reservoir rocks, a micro-continuum modeling framework has been developed to address the sub-resolution porosity in micro-CT images (Soulaine and Tchelepi, 2016). Such micro-continuum approaches consider the unresolved porous region (pore sizes below image resolution) as a continuum, and use Darcy's law for the fluid flow. The Stokes equation is used for the resolved pores and is coupled with the Darcy equation in the unresolved porous region based on the Darcy–Brinkman–Stokes equations (Brinkman, 1949). The porosity (ϕ) is used as an indicator to differentiate void space from the unresolved porous region ($\phi = 1$ represents void, $0 < \phi < 1$ represents sub-resolution porous region). Similar multiscale concepts have also been developed for pore network models (PNM) to address the subresolution microporosity (Mehmani and Prodanović, 2014; Bultreys et al., 2015). In the present work, we develop a micro-continuum modeling framework to model gas transport in organic-rich shale based on 3D digital images (obtained from micro-CT, nano-CT, or FIB-SEM; FIB-SEM images are used in our work). For pores that are resolved fully in the image, we model the gas flow with the Stokes equation. The unresolved regions, where the pore sizes are below the image resolution, are treated as a continuum (porous medium). For this nanoporous sub-resolution continuum, we develop an apparent permeability model that accounts for non-Darcy effects (i.e., slip flow and Knudsen diffusion), adsorption/desorption, and surface diffusion. The specific model for the nano-porous region depends on the types of material constituents segmented from the image (see Fig. 1). Here, the nano-porous region includes organic matter and clay; adsorption/desorption and surface diffusion are accounted for in the organic matter, but not in clay. The granular minerals, consisting of quartz, calcite, ankerite, albite, and pyrite for the sample we use, have negligible porosity and are considered impermeable (Ma et al., 2018).

The paper is organized as follows. In Section 2 we introduce the gas transport mechanisms and summarize current models for shale gas transport. Then, the micro-continuum framework is introduced. We apply the model to simulate a 3D FIB-SEM image (a subset of the image in Fig. 1) to compute the apparent permeability. We then simulate the transient gas production process. Analysis of the numerical experiments is presented in Section 4. Then, we discuss the implications of the analysis, the limitations of the model, and future directions in Section 5. We close with concluding remarks in Section 6.

2. Physics and modeling of shale gas transport

Gas transport in shale differs from that in conventional formations due to the extremely small (nanometer range) pores and the strong heterogeneity of organic-rich shale materials. Different mechanisms dominate the transport in different materials. Thus, models with different physics need to be applied to different material constituents of shale rock. In this section, we summarize the models for gas transport in complex shale material constituents. Note that our paper considers only a single-component - methane, and the term "gas" refers to methane.

2.1. Gas flow through straight tubes and idealized porous media

We summarize models for the rarefied gas flow in straight tubes with radial and rectangular cross-sections, and then extend the simple tube models to gas flow in idealized nano-porous media using the bundle-of-tubes representation.

2.1.1. Equation-of-state for free methane

The density and viscosity of methane vary with pressure and temperature. The density of free methane (ρ_f) can be expressed as

$$\rho_f = \frac{p_f M}{Z R T}, \tag{1}$$

where p_f is the pressure of free methane, M is the methane molecular weight, Z is the compressibility factor which equals to unity for ideal gas, R is the gas constant, and T is the absolute temperature. The subscript "f" denotes free gas.

The compressibility factor, Z, as an empirical function of pressure and temperature has been developed in the literature, which gives equations of state for density. Models for the viscosity of methane also exist in the literature. In our paper, we use the equation of state proposed by Mahmoud (2014) and the viscosity equation by Lee et al. (1966). These equations are presented in Appendix A.

2.1.2. Flow of free gas

Gas flow through nano- and micro-scale conduits leads to the so-called rarefaction effects, whereby the gas flow behavior deviates from the Navier–Stokes equations that are based on the continuum assumption. The deviation from the continuum approximation can be measured using the Knudsen number (Kn), which is the ratio between the mean free path (λ) and a characteristic length scale of the conduit (L) for free gas flow,

$$\mathrm{Kn} = \frac{\lambda}{L}, \tag{2}$$

where the mean free path λ is the average distance traveled by the gas molecules between collisions and has the following expression

$$\lambda = \frac{\mu_f}{p_f}\sqrt{\frac{\pi Z R T}{2M}}, \tag{3}$$

where μ_f is dynamic viscosity of free gas.

As the Knudsen number increases, the rarefaction effects become more important, and the flow cannot be predicted by models based on the continuum hypothesis, i.e., Navier–Stokes equations. Different models should be applied for gas flow in different flow regimes, as discussed in the introduction (continuum flow: $\mathrm{Kn} \lesssim 0.001$, slip flow: $0.001 < \mathrm{Kn} \lesssim 0.1$, transition flow: $0.1 < \mathrm{Kn} \lesssim 10$, free molecular flow: $\mathrm{Kn} > 10$). Here, we consider gas flow through a straight tube with a radial, or rectangular, cross-section, and briefly introduce the BK model, the unified model from Beskok and Karniadakis (1999), that is applicable to all flow regimes. In the BK model, the volumetric flux q_f through a tube can be written as the Hagen–Poiseuille flux $q_{\mathrm{H-P},f}$ multiplied by a correction factor, namely,

$$q_f = f(\mathrm{Kn}) q_{\mathrm{H-P},f}, \tag{4}$$

where the correction factor f(Kn) is a function of the Knudsen number and corrects for gas flow that deviates from continuum flow when Kn is large. For a radial tube, f(Kn) is given by

$$f(\mathrm{Kn}) = (1 + \alpha \mathrm{Kn})\left(1 + \frac{4\mathrm{Kn}}{1 - b\mathrm{Kn}}\right), \tag{5}$$

while for a rectangular tube, the correction factor is

$$f(\mathrm{Kn}) = (1 + \alpha \mathrm{Kn})\left(1 + \frac{6\mathrm{Kn}}{1 - b\mathrm{Kn}}\right), \tag{6}$$

where $\mathrm{Kn} = \lambda/r$ for a radial tube with r being the radius; $\mathrm{Kn} = \lambda/h$ for a rectangular tube with h being the height; $C_r(\mathrm{Kn}) = 1 + \alpha \mathrm{Kn}$ is the rarefaction coefficient that models the effect of reduced inter-molecular collisions with increased Kn; α is an coefficient that can be determined by experiments or from linearized Boltzmann solution; b is the slip coefficient and is determined as $b = -1$ for tube flow representing a second-order slip condition. For a radial tube, $q_{\mathrm{H-P},f} = \pi r^4/8/\mu_f$, while for a rectangular tube, $q_{\mathrm{H-P},f} = C(\mathrm{AR}) w h^3/12/\mu_f$ where w is the width of the rectangular cross-section and C(AR) is the correction factor for the geometry that is a function of the aspect ratio of the rectangular channel

(AR = w/h) and is independent of Kn. Note that $f(\mathrm{Kn}) \to 1$ as $\mathrm{Kn} \to 0$, and q_f recovers the Hagen–Poiseuille flux.

By comparing the volumetric flux predicted by Eqs. (5) and (6) with the linearized Boltzmann solution, α is fitted as an empirical analytical function $\alpha = \alpha_0(2/\pi)\tan^{-1}(\alpha_1 \mathrm{Kn}^{\beta})$ with two free parameters α_1 and β. α_0 is determined by equating the flux predicted from Eqs. (5) and (6) to the free molecular rate (Knudsen diffusion) when $\mathrm{Kn} \to \infty$.

The BK model works well for rarefied gas flow in straight tubes for all flow regimes ($0 \le \mathrm{Kn} < \infty$); however, a similar unified model has not been developed for complex natural porous media, which consist of many connected nano-scale pores and pore throats. Rarefied gas flow through porous medium with low permeability (tight rocks) was first systematically studied by Klinkenberg (1941). Klinkenberg (1941) derived a model for gas flow through a straight capillary tube with a correction of the slip boundary condition. He then introduced the so-called apparent gas permeability for flow through an idealized porous medium that consists of a bundle of capillary tubes with the same diameter. The apparent permeability can be written as a correction factor multiplied by the intrinsic permeability, k, as follows:

$$k_a = \left(1 + \frac{d}{\bar{p}}\right)k, \tag{7}$$

where d is a constant and $\bar{p}$ is the reciprocal mean gas pressure.

Civan (2010) used the BK tube model and derived a unified apparent permeability model for an idealized porous medium blue consisting of a bundle of tubes. Such model has a similar form as Eq. (7) by replacing $(1 + d/\bar{p})$ with $f(\mathrm{Kn})$

$$k_a = f(\mathrm{Kn})k, \tag{8}$$

where again k is the intrinsic permeability of the porous medium, which was given by the Kozeny–Carman model in Civan (2010).

We note that the bundle-of-nano-tubes model from Civan (2010) is a simplified apparent permeability model for a nano-porous medium and can overestimate the apparent permeability as reported by Landry et al. (2016). More sophisticated models may be developed by considering the complex pore structures observed in natural shale formations.

2.1.3. Adsorption/desorption and surface diffusion of adsorbed gas

The nano-tubes, or nano-porous materials, lead to extremely small pores and thus large surface areas on which gas can be adsorbed. The adsorbed gas may also migrate along the pore wall, which is often considered as a diffusion process that is named surface diffusion (Ruthven, 1984; Medveď and Černỳ, 2011). The amount of adsorption depends on the pressure and temperature of the free gas, and is often modeled by an isotherm that relates the amount of adsorption to the pressure of the free gas at a constant temperature. We discuss the details of the models for adsorbed gas in the following section when we consider specific shale material constituents.

2.2. Gas transport in shale

Digital images of shale show strong heterogeneity of the different material constituents (e.g., Fig. 1). In this section, based on the FIB-SEM images in Fig. 1, we consider four material constituents: macro-pores, organic matter, clay minerals, and granular minerals, and we employ different models for each of them. Organic matter and clay both contain very small unresolved pores that are below the image resolution. In these sub-resolution pores, non-Darcy effects (i.e., slip flow and Knudsen diffusion), adsorption/desorption, and surface diffusion can play important roles. We consider these unresolved regions as nano-porous materials with connected sub-resolution pores and pore throats, and model the various gas transport mechanisms at the continuum scale. Here, we use the simple bundle-of-nano-tubes model for the unresolved nano-porous regions. The granular minerals have negligible porosity, allowing us to consider them as impermeable materials, i.e., zero porosity and zero permeability. The macro-pores are pores that are fully resolved in the image; these macro-pores may belong to organic matter, clay minerals, or granular minerals. They can also bridge these three constituents. We model gas transport in macro-pores using the Stokes equation. This is justified based on the assumption that the macro-pores have large sizes such that that the flow is either in the continuum flow regime, or the slip flow regime, where the Navier–Stokes equations (with velocity slip conditions) are applicable.

2.2.1. Gas transport in organic matter

We consider the organic matter with sub-resolution pores as a nano-porous medium, and derive an apparent permeability model based on Section 2.1. In addition, we consider gas adsorption and surface diffusion.

Model for the apparent permeability

The organic matter has mostly circular pores and pore throats (see for example the HIM images in Wu et al., 2017). For the apparent permeability, we use the correction function from the bundle-of-nano-tubes model derived from the BK model for radial tubes. Thus, we have

$$f(\mathrm{Kn}) = (1 + \alpha_{\mathrm{om}}\mathrm{Kn})\left(1 + \frac{4\mathrm{Kn}}{1 + \mathrm{Kn}}\right), \tag{9}$$

where $\alpha_{\mathrm{om}} = a_{0,\mathrm{om}}\frac{2}{\pi}\tan^{-1}\left(\alpha_{1,\mathrm{om}}\mathrm{Kn}^{\beta_{\mathrm{om}}}\right)$ with $a_{0,\mathrm{om}} = \frac{64}{15\pi}$, $\alpha_{1,\mathrm{om}} = 4.0$, $\beta_{\mathrm{om}} = 0.4$. The subscript "om" denotes organic matter.

Then, using the correction function, flow of free gas in the organic matter can be described by the Darcy-type equation with an apparent permeability $k_{a,\,\mathrm{om}}$ as

$$\mathbf{u}_f = -\frac{k_{a,\mathrm{om}}}{\mu_f}\nabla p_f = -\frac{(1 + \alpha_{\mathrm{om}}\mathrm{Kn})\left(1 + \frac{4\mathrm{Kn}}{1+\mathrm{Kn}}\right)k_{\mathrm{om}}}{\mu_f}\nabla p_f. \tag{10}$$

Since the sub-resolution pores in the organic matter are not resolved in the image, we need to make approximations for the porosity, permeability, and the average pore radius. Some of the information can be estimated from higher resolution TEM, or HIM, images of the organic matter and the pore size distribution measured from nitrogen adsorption. We obtain the Kn number based on the average radius and compute the intrinsic permeability k_{om} using the Kozeny–Carman model using the estimated porosity.

Experiments have shown that the Langmuir isotherm fits methane adsorption in organic-rich shale and isolated kerogen reasonably well (Heller and Zoback, 2014; Rexer et al., 2014). As a result, we use the Langmuir isotherm to model methane adsorption in the organic matter.

$$n_{\mathrm{ad}} = n_{\mathrm{ad}}^{\max}\frac{Kp_f}{1 + Kp_f}, \tag{11}$$

where n_{ad} is the amount of adsorbed gas (mass per unit volume of porous material), $n_{\mathrm{ad}}^{\max}$ is the maximum adsorption, K is the Langmuir coefficient, which is the inverse of the pressure at which half of the adsorption sites are occupied.

Surface diffusion

The adsorbed methane can migrate along the pore wall through a process referred to as surface diffusion (Ruthven, 1984; Medveď and Černỳ, 2011). The volumetric flux of the adsorbed gas in organic matter due to surface diffusion can be written as

$$\mathbf{u}_{\mathrm{ad}} = -\frac{1}{\rho_{\mathrm{ad}}}D_s\nabla n_{\mathrm{ad}} = -\frac{1}{\rho_{\mathrm{ad}}}D_s\nabla\left(n_{\mathrm{ad}}^{\max}\frac{Kp_f}{1 + Kp_f}\right), \tag{12}$$

where $\boldsymbol{u}_{\mathrm{ad}}$ is the volumetric flow rate per unit area, ρ_{ad} is the density of the adsorbed gas, D_s is the surface diffusivity. Note that we assume the diffusion is isotropic and thus D_s is a scalar.

2.2.2. Gas transport in clay

Here, we discuss the gas flow model in clay, which is also modeled as a nano-porous medium with sub-resolution pores. Gas adsorption in clay may be negligible due to the presence of water in natural shale formations (see Zhang et al., 2012; Rexer et al., 2014). Thus, we do not consider gas adsorption effects in clay. When adsorption is considered in clay, swelling mechanisms may need to be modeled (e.g., Bakhshian et al., 2018). Unlike the circular pores in organic matter, clay has slit-like pores; as a result, we use the correction function from the bundle-of-nano-tubes model derived from the BK model for rectangular tubes. Namely,

$$f(\mathrm{Kn}) = (1+\alpha_c \mathrm{Kn})\left(1+\frac{6\mathrm{Kn}}{1+\mathrm{Kn}}\right). \tag{13}$$

where α_c follows the same empirical relation as in the radial tube case, with different coefficients $\alpha_{0,\,c}$, $\alpha_{1,\,c}$, and β_c that change with the aspect ratio (AR = w/h) of the rectangular tube. The subscript "c" represents clay.

Then, the volumetric flux of free gas in clay becomes

$$\mathbf{u}_f = -\frac{k_{a,c}}{\mu_f}\nabla p_f = -\frac{(1+\alpha_c \mathrm{Kn})\left(1+\frac{6\mathrm{Kn}}{1+\mathrm{Kn}}\right)k_c}{\mu_f}\nabla p_f. \tag{14}$$

where $k_{a,\,c}$ and k_c are the apparent permeability and intrinsic permeability of clay, respectively.

Similar to the organic matter, we obtain Kn using the estimated average pore thickness in clay. The intrinsic permeability k_c of clay is approximated with the Kozeny–Carman model with estimated porosity.

2.2.3. Gas transport in macro-pores

We assume that the macro-pores have large sizes that the flow is either in the continuum flow regime, or the slip flow regime where the Navier–Stokes equations (with velocity slip conditions) are applicable. Shale is known to have very low permeability (from nanoDarcy to microDarcy); therefore, we neglect inertial effects and use the Stokes equation to model gas flow in the macro-pores. We use the following equation for compressible flow in the macropore (see Appendix B for a scaling argument).

$$0 = -\nabla p_f + \rho_f \mathbf{g} + \nabla\cdot\left(\mu_f \nabla \mathbf{u}_f\right) + \frac{1}{3}\nabla\left(\mu_f \nabla\cdot\mathbf{u}_f\right). \tag{15}$$

By considering appropriate velocity slip conditions at the wall of the macro-pores, the Stokes equation is applicable for both the continuum flow regime and the slip flow regime.

3. Micro-continuum modeling framework

We cast the models for gas transport in the different material constituents (organic matter, clay minerals, macro-pores, and granular minerals) into a micro-continuum modeling framework (Soulaine and Tchelepi, 2016). The micro-continuum framework allows us to solve Stokes flow in the macro-pores and continuum-scale flow in the nanoporous organic matter and clay without explicit coupling at the boundaries between the different constituents. It has been shown that the single-momentum equation approach is a good approximation of the explicit coupling between Stokes and Darcy equations using the Beavers–Joseph condition (Beavers and Joseph, 1967; Goyeau et al., 2003). We present the mathematical model and the numerical algorithm in the following.

3.1. Mathematical model

The micro-continuum modeling framework is based on the Darcy–Brinkman–Stokes equations (Brinkman, 1949), which have been recently used to model fluid flow in reservoir rocks at the pore-scale, such as carbonate (Scheibe et al., 2015; Soulaine and Tchelepi, 2016).

We consider compressible flow using the equation of states from Section 2.1.1. The mass balance equation for methane, including both the free and adsorbed phases, can be written as

$$\frac{\partial(\phi\rho_f)}{\partial t} + \delta_{\mathrm{om}}\frac{\partial}{\partial t}\left[\left(1-\frac{\rho_f}{\rho_{\mathrm{ad}}}\right)n_{\mathrm{ad}}\right] + \nabla\cdot\left(\rho_f \mathbf{u}_f + \delta_{\mathrm{om}}\rho_{\mathrm{ad}}\mathbf{u}_{\mathrm{ad}}\right) = 0 \tag{16}$$

where ϕ is the porosity, which is between 0 and 1 in the region with sub-resolution pores (i.e., organic matter and clay). The porosity is zero in granular minerals and unity in macro-pores; δ_{om} is an indicator for the organic matter, $\delta_{\mathrm{om}} = 1$ when it is in the organic matter, otherwise $\delta_{\mathrm{om}} = 0$. We multiply the terms associated with adsorption by δ_{om} because we only consider adsorption/desorption in the organic matter. We note that the adsorbed gas occupies a fraction of the porosity that would otherwise be filled with free gas. The reduction of the porosity due to adsorption needs to be taken into account (Heller and Zoback, 2014) by using the excess adsorption, $(1-\frac{\rho_f}{\rho_{\mathrm{ad}}})n_{\mathrm{ad}}$, which is defined as the absolute adsorption n_{ad} subtracted by the mass of the free gas that is replaced by the adsorbed gas, $\frac{\rho_f}{\rho_{\mathrm{ad}}}n_{\mathrm{ad}}$.

For the momentum equation, we use the compressible Darcy–Brinkman–Stokes equation to link the models for gas transport in the organic matter, clay, and macro-pores (see Eq. (17)). Eq. (17) recovers Eq. (15) in the macro-pores, and recovers the Darcy-type equation $\mathbf{u}_f = -\frac{k_a}{\mu_f}\nabla p_f$ in the nano-porous region with sub-resolution pores. We note that the permeability k_a is not only a function of the pore structure, it also depends on the flow properties, e.g., Kn number, and follows Eqs. (10) and (14) in the organic matter and clay regions, respectively. We consider no-slip condition at the interface between the macro-pores and the granular minerals.

$$0 = -\nabla p_f + \rho_f \mathbf{g} + \frac{1}{\phi}\nabla\cdot\left(\mu_f\nabla\mathbf{u}_f\right) + \frac{1}{3\phi}\nabla\left(\mu_f\nabla\cdot\mathbf{u}_f\right) - \mu_f k_{\mathrm{a}}^{-1}\mathbf{u}_f. \tag{17}$$

3.2. Numerical algorithm

We implement and solve the set of equations for the micro-continuum framework (Eqs. (16) and (17)) in OpenFOAM® based on the PIMPLE solver, which is a transient solver for the Navier–Stokes equations that merges the PISO (Pressure Implicit Splitting Operator) (Issa, 1986) and SIMPLE (Semi-Implicit Method of Pressure-Linked Equations) algorithms (Patankar, 1980). We present the details of the discretization and the PIMPLE algorithm to solve Eqs. (16) and (17) in Appendix C.

4. Results and analysis

Now, we use the micro-continuum pore-scale model to analyze how different physical transport mechanisms describe the overall transport in complex 3D models of shale based on high-resolution images of the shale pore structures and material constituents. We design two types of numerical experiments. One uses periodic boundary conditions, where we are interested in computing the overall flow capacity of the sample (i.e., the apparent permeability). The other setting uses Dirichlet boundary conditions to simulate the transient process of gas production. In both cases, the left and/or the right faces of the sample are open for flow and the other four sides of the sample are closed (see Fig. 2). To analyze the importance of different physics or transport mechanisms, we consider four levels of model complexity:

(1) Darcy + Stokes (DS): gas flow in organic matter and clay is modeled with Darcy's law, and Stokes equation is used for flow in macro-pores;
(2) Darcy + Stokes + adsorption/desorption (DSA): adsorption/desorption is considered in organic matter in addition to the DS model;
(3) nonDarcy + Stokes + adsorption/desorption (NDSA): non-Darcy effects are included in both organic matter and clay, with everything else the same as the DSA model;

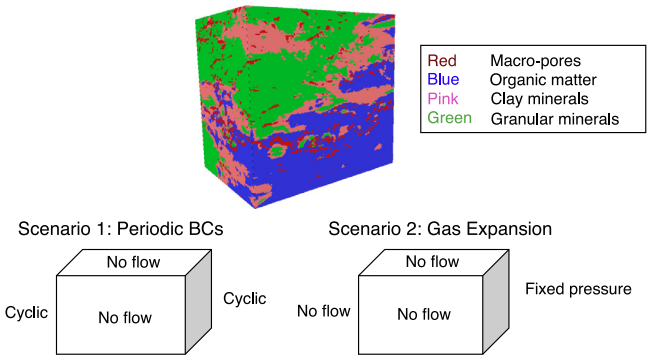

Fig. 2. Sketches of two numerical experiments for simulating gas transport on a 3D FIB-SEM image. In both scenarios, left and/or right boundaries are open for flow and the other four sizes are no-flow boundaries. The first scenario considers periodic boundary conditions to compute an apparent permeability, and the second scenario only allows the right boundary to be open at a fixed pressure (p_{f_2}) that is lower than the initial pressure in the sample ($p_{f_1} = p_{f_2} + \Delta p$). The difference between the two pressures is small, $\Delta p \ll p_{f_2}$.

(4) nonDarcy + Stokes + adsorption/desorption + surface diffusion (full model): this refers to the NDSA model with effects due to surface diffusion of the adsorbed methane.

In the following subsections, we introduce the FIB-SEM images. Then we present the simulation results and analysis for the two numerical experiments and for all of the four models.

4.1. FIB-SEM images used for the flow simulations

We use a subset of the original image shown in Fig. 1 for our pore-scale simulation. This is because using the original full image is computationally expensive and becomes prohibitive for our detailed analysis. The sub-image is cut with each dimension being about half of the original full image. The size of the sub-image is $L_x = 3.56\,\mu$m, $L_y = 2.50\,\mu$m, $L_z = 3.36\,\mu$m, and the voxel size is the same as the original full image ($\Delta x = \Delta y = 10$ nm, $\Delta z = 20$ nm). Fig. 3 shows distributions of the four material constituents in the sub-image. We also identify the two largest connected macro-pore clusters in Fig. 3(f), which shows that there is a macro-pore network (the largest cluster) connecting the left face to the right face of the image. We will see later that this pore structure has a significant impact on the results of the simulations. The 3D images were acquired in a Dual Beam FIB-SEM (Nova NanoLab 600i, FEI, Hillsboro, United States) and they were aligned and sheared as a series of block face images before segmentation. A band-pass filter, non-local means filter, sober filter and a top-hat filter were applied for the minerals, organic matter and pores segmentation. More details about the shale core sample, the acquisition procedures of the image, the image processing and other measurements can be found in Ma et al. (2018)

We discretize the image with the finite-volume scheme and solve Eqs. (16) and (17) subject to the boundary conditions of the two numerical experiments. The numerical grid cells have a one-to-one correspondence with the digital voxels of the image, which leads to 14,952,000 grid cells. Each voxel belongs to one of the four material constituents, and is given a porosity. Voxels with $\phi = 1$ belong to macro-pores, $\phi = 0$ belong to granular minerals, and $\phi \in (0, 1)$ represents organic matter and clay. $\delta_{\text{om}} = 1$ when a voxel sits in organic matter, otherwise, $\delta_{\text{om}} = 0$.

4.2. 3D simulations with periodic BCs: computing apparent permeability

In this section, we present the results and analysis of the first numerical experiment, which includes two parts. The first part computes and analyzes the apparent permeability of organic matter and clay, and the second part considers the apparent permeability of the 3D image.

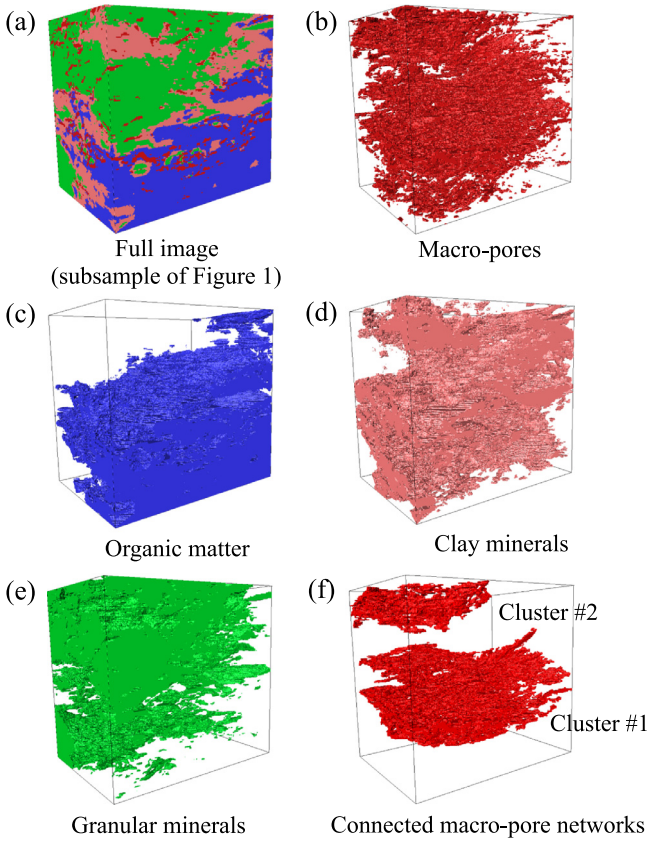

Fig. 3. A subsample of the full image in Fig. 1. Size of the image: 3.56 μm × 2.50 μm × 3.36 μm. (a) shows the overall image, and (b)–(e) show the distributions of the four material constituents: red - macro-pores, blue - organic matter, pink - clay minerals, green - granular minerals; (f) shows the two largest connected macro-pore networks.(For interpretation of the references to color in this figure legend, the reader is referred to the web version of this article.)

Table 1
Parameters used for the simulations. Note that organic matter is assumed to have radial pores and the average pore size is the average pore radius; clay is assumed to have slit-like pores and the average pore size refers to the average pore thickness.

Parameter	Value
Porosity of organic matter (ϕ_{om})	0.1
Porosity of clay (ϕ_c)	0.1
Average pore size in organic matter	5 nm
Average pore size in clay	5 nm
Langmuir coefficient (K)	4×10^{-8} Pa^{-1}
Maximum adsorption ($n_{\text{ad}}^{\max}$)	44.8 kg/m^3
Surface diffusion coefficient (D_s)	See Table 2
Density of adsorbed gas (ρ_{ad})	400 kg/m^3
Temperature	400 K

Here, we introduce the parameters we use for the simulation (see Table 1). The organic matter and the clay are assumed to be homogeneous with a porosity of 0.1. The organic matter has an average pore radius of 5 nm and the clay slit-pores have an average height of 5 nm. The equation of state and the viscosity equation of methane give the density and viscosity range from $p = 1$ MPa to $p = 50$ MPa (see Fig. 4). Details of the equation of state and viscosity equation are shown in Appendix A. We consider an isothermal system with a temperature of 400 K. As we can see, density of methane changes drastically from $p = 1$ MPa to $p = 50$ MPa, while the viscosity has much less variation. The critical

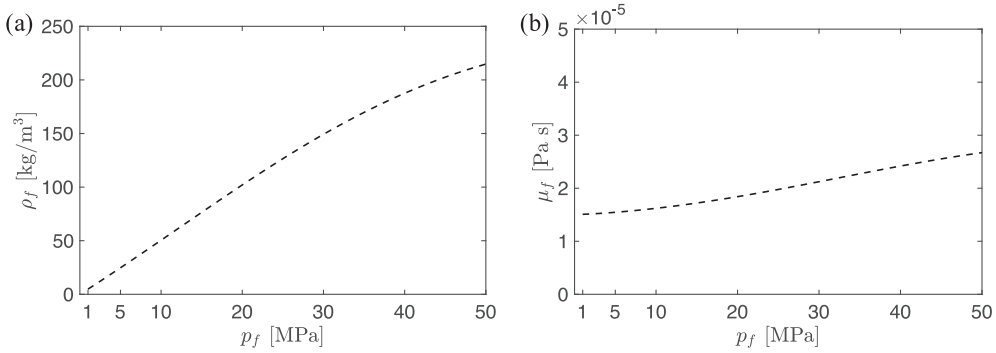

Fig. 4. Variations of density (a) and viscosity (b) of methane with gas pressure.

Table 2
Surface diffusion coefficient as function of gas pressure.

p_f [MPa]	1	5	10	20	30	40	50
D_s [10^{-8} m^2/s]	8.32×10^{-1}	9.52×10^{-1}	1.14	1.44	1.77	2.10	2.46

pressure of methane $p_{\text{critical}} = 4.599$ MPa and the critical temperature $T_{\text{critical}} = 190.564$ K. At $T = 400$ K, methane enters the supercritical phase when pressure is higher than the critical pressure $p_{\text{critical}} = 4.599$ MPa. The Langmuir coefficient, maximum adsorption, and density of adsorbed gas are typical parameters for isolated organic matter obtained from Rexer et al. (2014). The surface diffusion coefficient (D_s) is a function of the amount of adsorption, and therefore depends on pressure. Here we take typical values from Medveď and Černý (2011) as shown in Table 2. $D_s = D_{s0} D_s / D_{s0}$, where $D_{s0} = 8.00 \times 10^{-9}$ m^2/s, and the ratio D_s/D_{s0} is taken from the Langmuir/HIO curve in Fig. 4 of Medveď and Černý (2011). We note that these parameters are typical parameters for surface diffusion in activated carbon obtained from the literature, though different parameters can be used, we do not expect that they change the qualitative behavior of the simulations.

4.2.1. Apparent permeability of clay and organic matter

The apparent permeability of organic matter and clay can be computed analytically from the models presented in Section 2.2.

The apparent permeability of clay can be obtained from Eq. (14) as:

$$k_{a,\text{c}} = (1 + \alpha_{\text{c}}\text{Kn})\left(1 + \frac{6\text{Kn}}{1+\text{Kn}}\right)k_{\text{c}}, \tag{18}$$

where $\alpha_{\text{c}} = \alpha_{0,\text{c}} \frac{2}{\pi} \tan^{-1}\left(\alpha_{1,\text{c}}\text{Kn}^{\beta_{\text{c}}}\right)$ with $\alpha_{0,\text{c}} = 1.5272$, $\alpha_{1,\text{c}} = 2.5$, $\beta_{\text{c}} = 0.5$. The coefficients $\alpha_{0,\text{c}}$, $\alpha_{1,\text{c}}$, and β_{c} are parameters for a rectangular tube with an aspect ratio of 4 ($w/h = 4$) (Beskok and Karniadakis, 1999). Here, we assume the clay pores have an averaged aspect ratio of 4. Different aspect ratio leads to different coefficients, but only with a slight modification to α_{c}. The intrinsic permeability of clay k_{c} is obtained using the Kozeny–Carman model with an average porosity of 0.1. We recognize that the Kozeny–Carman model may not be applicable to the clay with slit-like pores, the idea here is to assign a reasonable intrinsic permeability to the clay minerals. A better intrinsic permeability may be assigned if higher resolution images of the nano-porous clay region are available.

The apparent permeability of the organic matter is more complex, since it involves the flux of the adsorbed gas (surface diffusion). To include surface diffusion, we convert the mass flux of the adsorbed gas into volumetric flux of free gas and combine it with the free gas flux to obtain the apparent permeability

$$k_{a,\text{om}} = -\left(\mathbf{u}_f + \mathbf{u}_{\text{ad}}\frac{\rho_{\text{ad}}}{\rho_f}\right)\mu_f/\nabla p_f = (1+\alpha_{\text{om}}\text{Kn})\left(1+\frac{4\text{Kn}}{1+\text{Kn}}\right)k_{\text{om}} + \frac{1}{\rho_f}\mu_f D_s n_{\text{ad}}^{\max}\frac{K}{(1+Kp_f)^2}, \tag{19}$$

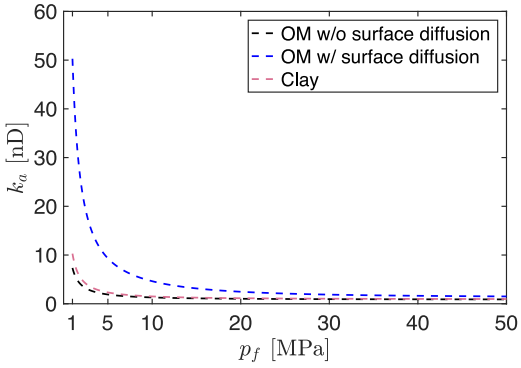

Fig. 5. Apparent permeability of organic matter and clay as a function of gas pressure. (For interpretation of the references to color in this figure legend, the reader is referred to the web version of this article.)

where $\alpha_{\text{om}} = \alpha_{0,\text{om}} \frac{2}{\pi} \tan^{-1}\left(\alpha_{1,\text{om}}\text{Kn}^{\beta_{\text{om}}}\right)$ with $\alpha_{0,\text{om}} = 1.358$, $\alpha_{1,\text{om}} = 4.0$, $\beta_{\text{om}} = 0.4$ (Beskok and Karniadakis, 1999). Similar to clay, the intrinsic permeability of organic matter k_{om} is obtained with the Kozeny–Carman model with an average porosity of 0.1. Here we compute the apparent permeability of organic matter both with and without surface diffusion.

From Eqs. (18) and (19), we plot the apparent permeability for clay and organic matter in Fig. 5 as a function of gas pressure. The intrinsic permeabilities k_{c} and k_{om} are both 0.69 nD (nD denotes nano Darcy, which is 10^{-21} m^2). The apparent permeabilities are a strong function of pressure that have arge values at $p_f = 1$ MPa and then quickly decrease for higher pressures. At $p_f = 1$ MPa, $k_{\text{c}} = 10.29$ nD, $k_{\text{om}} = 7.35$ nD without surface diffusion, and $k_{\text{om}} = 50.28$ nD when surface diffusion is included; at $p_f = 50$ MPa, $k_{\text{c}} = 0.97$ nD, $k_{\text{om}} = 0.90$ nD without surface diffusion, and $k_{\text{om}} = 1.51$ nD when surface diffusion is included. We can see that surface diffusion significantly increases the apparent permeability of the organic matter at low pressure ($\sim$7 times of the apparent permeability without surface diffusion at $p_f = 1$ MPa); surface diffusion effects become less important for high pressures ($\sim$1.7 times of the apparent permeability without surface diffusion at $p_f = 50$ MPa).

4.2.2. Apparent permeability of the 3D sample

Now we take the image (Fig. 3) and compute the apparent permeability of the entire sample using periodic boundary conditions shown in Fig. 2. We include a body force in the momentum equation to impose a pressure gradient in x direction, and then solve Eqs. (16) and (17) sub-

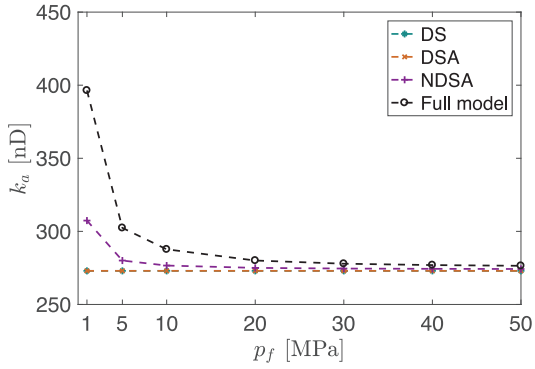

Fig. 6. Apparent permeability of the 3D image in x direction computed from the four models (DS, DSA, NDSA, and full model) using periodic BCs for gas pressures $p_f = 1, 5, 10, 20, 30, 40, 50$ MPa.

ject to the periodic boundary conditions in x direction until it reaches steady state. The pressure gradient we assign is $\partial p_f/\partial x = 10^5$ Pa/m. We use q to denote the volumetric flow rate through the y–z cross-section of the sample at steady state, which can be obtained as

$$q = \int u_x \mathrm{d}y\mathrm{d}z. \tag{20}$$

Then, the apparent permeability of the sample in x direction can be defined as

$$k_{a,\mathrm{sample},x} = q \Big/ \left[(L_y L_z)\mu_f \frac{\partial p_f}{\partial x} \right]. \tag{21}$$

We assign a reference pressure to the domain to compute an apparent permeability for a given pressure. The reference pressure is set at the right boundary, and the maximum difference of the pressure in the domain relative to the reference pressure is negligibly small, $L_x \partial p_f/\partial x = 0.356$ Pa. We compute the apparent permeability for reference pressures $p_f = 1, 5, 10, 20, 30, 40, 50$ MPa, for all of the four models (DS, DSA, NDSA, and full model). Note that $q = q_f$ for the first three models (DS, DSA, NDSA) where there is only free gas flux, while $q = q_f + q_{\mathrm{ad}} \frac{\rho_{\mathrm{ad}}}{\rho_f}$ for the full model where surface diffusion is included.

We summarize the computed apparent permeabilities in Fig. 6, from which we can make several observations. First, because of the connected macro-pore network (Fig. 3(f)), the permeability of the sample from the DS model ($k_{\mathrm{DS}} = 272.98$ nD) is much larger than the intrinsic permeability of clay and organic matter (0.69 nD). Second, $k_{\mathrm{DSA}} = k_{\mathrm{DS}}$ since adsorption does not change permeability at steady state. Third, apparent permeabilities from the NDSA model and full model are higher, especially at low pressure, $k_{\mathrm{NDSA}} = 307.38$ nD and $k_{\mathrm{full\,model}} = 396.41$ nD at $p_f = 1$ MPa. However, the increase relative to the DS permeability (less than $\sim$1.5 times of k_{DS}) is much smaller compared to the increase of the apparent permeability of clay and organic matter relative to their intrinsic permeability (see Fig. 5). This again shows that the connected macro-pore network completely dominates the permeability of the sample, which undermines the enhancement of flow capacity from non-Darcy effects and surface diffusion.

4.3. 3D simulations of gas expansion: simulating gas production

In this section, we present the second numerical experiment where we model gas expansion to simulate gas production. Before we show the simulation results, we introduce a simplified one-dimensional (1D) model for our system, which will be used to interpret the results of the 3D simulations.

4.3.1. One-dimensional model for gas expansion

Because only the right boundary of the domain is open for flow in our gas expansion system, it may be reasonable to approximate gas production as a 1D problem. This 1D model is similar to the flow model for pressure-pulse decay method (Brace et al., 1968; Dicker and Smits, 1988; Cui et al., 2009). For simplicity, we assume homogeneous properties of the domain. The porosity of the sample is $\bar{\phi}$ and the volume fraction of organic matter is $\bar{\gamma}_{\mathrm{om}}$. The sample has an apparent permeability $\bar{k}_a$ when surface diffusion is not included. Here we consider surface diffusion separately. Then, the mass balance equation of the 1D model can be written as

$$\frac{\partial\left(\bar{\phi}\rho_f\right)}{\partial t} + \bar{\gamma}_{\mathrm{om}} \frac{\partial}{\partial t}\left[\left(1 - \frac{\rho_f}{\rho_{\mathrm{ad}}}\right) n_{\mathrm{ad}}\right] + \frac{\partial\left(\rho_f u_{f,x} + \bar{\gamma}_{\mathrm{om}} \rho_{\mathrm{ad}} u_{\mathrm{ad},x}\right)}{\partial x} = 0. \tag{22}$$

The pressure boundary condition only introduces a small pressure perturbation to the domain ($\Delta p = p_{f_1} - p_{f_2} \ll p_{f_2}$), so that Eq. (22) can be considered as a linear equation. Rearranging Eq. (22), we obtain a linear 1D diffusion equation

$$\frac{\partial p_f}{\partial t} = \hat{k} \frac{\partial^2 p_f}{\partial x^2}, \tag{23}$$

where

$$\hat{k} = \left[\rho_f \frac{\bar{k}_a}{\mu_f} + \bar{\gamma}_{\mathrm{om}} D_s n_{\mathrm{ad}}^{\max} \frac{K}{\left(1 + K p_f\right)^2} \right] \Big/ \left[\bar{\phi} \frac{\partial \rho_f}{\partial p_f} + \bar{\gamma}_{\mathrm{om}} \left(1 - \frac{\rho_f}{\rho_{\mathrm{ad}}}\right) n_{\mathrm{ad}}^{\max} \frac{K}{\left(1 + K p_f\right)^2} - \bar{\gamma}_{\mathrm{om}} \frac{n_{\mathrm{ad}}^{\max} K p_f}{\rho_{\mathrm{ad}}\left(1 + K p_f\right)} \frac{\partial \rho_f}{\partial p_f} \right]. \tag{24}$$

The initial and boundary conditions are

$$p_f(x, t = 0) = p_{f_1}, \tag{25}$$

$$\frac{\partial p_f}{\partial x}(x = 0, t) = 0, \tag{26}$$

$$p_f(x = L_x, t) = p_{f_2}. \tag{27}$$

The details of the derivations from Eq. (22) to Eq. (23) are presented in Appendix D.

Now, we cast Eq. (23) in dimensionless form by defining $P_f = \frac{p_f - p_{f_2}}{p_{f_1} - p_{f_2}}$, $X = x/L_x$, $T = t/\left(L_x^2/\hat{k}_{\mathrm{DS}}\right)$, where $\hat{k}_{\mathrm{DS}}$ is the diffusivity from Eq. (23) when the DS model is considered (i.e., neglecting non-Darcy effects, adsorption/desorption, and surface diffusion), which has the following form

$$\hat{k}_{\mathrm{DS}} = \frac{\rho_f \frac{k_{\mathrm{DS}}}{\mu_f}}{\bar{\phi} \frac{\partial \rho_f}{\partial p_f}}. \tag{28}$$

Substitution of the dimensionless variables into Eq. (23) gives

$$\frac{\partial P_f}{\partial T} = \frac{\hat{k}}{\hat{k}_{\mathrm{DS}}} \frac{\partial^2 P_f}{\partial X^2}. \tag{29}$$

The corresponding dimensionless boundary conditions become

$$P_f(X, T = 0) = 1, \tag{30}$$

$$\frac{\partial P_f}{\partial X}(X = 0, T) = 0, \tag{31}$$

$$P_f(X = 1, T) = 0. \tag{32}$$

For a small pressure perturbation at the right boundary, $\frac{\hat{k}}{\hat{k}_{\mathrm{DS}}}$ can be considered as a constant, then Eq. (29) subject to the initial and boundary conditions (30)–(32) can be solved analytically

$$P_f = \sum_{n=0}^{\infty} \frac{2}{(n + 1/2)\pi} \sin\left[(n + 1/2)\pi(1 - X)\right] e^{-(n+1/2)^2 \pi^2 \frac{\hat{k}}{\hat{k}_{\mathrm{DS}}} T}. \tag{33}$$

Approximating P_f using the first term of the series solution (33) gives

$$P_f = \frac{4}{\pi}\sin\left(\frac{1}{2}\pi(1-X)\right)e^{-\frac{1}{4}\pi^2\frac{\hat{k}}{k_{\mathrm{DS}}}T}. \tag{34}$$

From the pressure solution Eq. (34), we can derive the expression for the outlet mass flow rate (production rate) at the right boundary. We nondimensionalize the outlet mass flow rate by $\dot{m}_{\mathrm{DS}} = -\rho_f \frac{k_{\mathrm{DS}}}{\mu_f}\frac{p_{f_2}-p_{f_1}}{L_x}$, the characteristic outlet mass flow rate from the DS model, and obtain the dimensionless outlet mass flow rate (not including surface diffusion) as

$$\dot{M} = \dot{m}/\dot{m}_{\mathrm{DS}} = -\frac{\bar{k}_a}{k_{\mathrm{DS}}}\frac{\partial P_f}{\partial X}|_{X=1} = 2\frac{\bar{k}_a}{k_{\mathrm{DS}}}e^{-\frac{1}{4}\pi^2\frac{\hat{k}}{k_{\mathrm{DS}}}T}. \tag{35}$$

When surface diffusion is included, the dimensionless outlet mass flow rate becomes

$$\begin{aligned}\dot{M} &= \dot{m}/\dot{m}_c \\ &= \frac{\left[\rho_f u_{f,x} + \rho_{\mathrm{ad}} u_{\mathrm{ad},x}\right]|_{X=1}}{\dot{m}_c} \\ &= 2\left[\frac{\bar{k}_a}{k_{\mathrm{DS}}} + \bar{\gamma}_{\mathrm{om}} D_s n_{\mathrm{ad}}^{\max}\frac{K\mu_f}{\rho_f k_{\mathrm{DS}}\left(1+Kp_f\right)^2}\right]e^{-\frac{1}{4}\pi^2\frac{\hat{k}}{k_{\mathrm{DS}}}T}.\end{aligned} \tag{36}$$

Eqs. (35) and (36) show that the dimensionless outlet mass flow rate declines exponentially with dimensionless time, T. $\ln \dot{M} \sim T$ with the slope $-\frac{1}{4}\pi^2\frac{\hat{k}}{k_{\mathrm{DS}}}$ representing the flow capacity of the shale sample. In the following section, we use the results and analysis of the 1D model to interpret the production decline results from the 3D simulations of gas production.

4.3.2. Production decline

We simulate gas production for $p_f = 1$ MPa and $p_f = 50$ MPa, representing low and high pressures, respectively. Pressure p_f refers to the gas pressure at the right boundary p_{f_2}. The difference between the initial pressure (p_{f_1}) in the domain and the boundary pressure (p_{f_2}) is kept as $\Delta p = 100\,\mathrm{Pa} \ll p_f$. Integrating the mass flux across the right boundary, we obtain the outlet mass flow rate. We normalize the mass flow rate using the characteristic mass flow rate from the DS model, $\dot{m}_{\mathrm{DS}}$, introduced in Section 4.3.1, and nondimensionalize the time scale using the characteristic time scale from the DS model, $T_{\mathrm{DS}} = L_x^2/\hat{k}_{\mathrm{DS}}$. Then, we plot the dimensionless mass flow rate with the dimensionless time on a semi-log scale, for both early time ($0 < T < 0.1$) and late time ($0 < T < 10$) (see Fig. 7).

Now we analyze the 3D gas production decline results using the 1D model in Section 4.3.1. We first look at the early time behavior. At $p_f = 1$ MPa, starting from $T \approx 0.05$, the production rates decline linearly in the semi-log scale and follow a similar slope in all of the four models (see Fig. 7 (a)), despite their very different model complexities. This is primarily due to the macro-pore network in the 3D image which connects the left boundary to the right boundary of the image, as shown in Fig. 3(f). The macro-pore network dominates gas production in early time, in which gas flow follows Stokes equation in any of the four models. Therefore, the four models share a similar slope in early time even though they have very different physics. We note that the gas production rates do not decline linearly in the very beginning up to $T \approx 0.05$. This is because the pressure signal at the right boundary has not reached the left boundary yet, and the system transits from a "semi-infinite" like domain to a finite domain, which does not follow the exponential scaling derived from the 1D model in Section 4.3.1. At $p_f = 50$ MPa, the production decline curves follow the same slope starting from $T \approx 0.05$ (see Fig. 7(b)). In addition, the production rates from the four models almost overlap with each other. We note that the production decline curves from the DS model for $p_f = 1$ MPa and $p_f = 50$ MPa are almost identical, which shows that the impact from compressibility is eliminated through the nondimensionalization.

In late time, the production decline curves from low and high gas pressures are quite different (see Fig. 7 (b) and (d)). At $p_f = 1$ MPa, the production rates from the four models diverge and follow very different decline slopes. The DS and DSA models have similar slopes with the DSA slope being slightly smaller. The NDSA model has a larger slope, and the full model has the largest slope. This is because gas production in late time is dominated by gas transport in the sub-resolution nano-porous region. The DS and DSA models both use Darcy's law in the nano-porous region. The DSA model includes adsorption which gives a smaller diffusivity $\hat{k}$ in the 1D model, then a flatter slope $-\frac{1}{4}\pi^2\frac{\hat{k}}{k_{\mathrm{DS}}}$. NDSA considers non-Darcy effects in both organic matter and clay, and therefore has a larger apparent permeability $\bar{k}_a$, which leads to a faster decline in production. In addition to the non-Darcy effects, the full model includes surface diffusion which further enhances gas transport in nano-porous region, as shown by the steepest decline curve. At $p_f = 50$ MPa, the production decline curves from the four models are almost indistinguishable. The full model has a slightly larger slope, while the DSA model has the smallest slope. This implies that the non-Darcy effects and surface diffusion are negligible at high pressures, which is consistent with our observation in the periodic BCs numerical experiment (Fig. 5). Again, we note that the production decline curves from the DS model for $p_f = 1$ MPa and $p_f = 50$ MPa are almost identical.

Finally, we point out that the transient analysis of gas production appears to be much more informative than the steady-state apparent permeability computed in Section 4.2. The apparent permeability can be considered as a lumped average of the flow capacity of the sample over time, while the transient gas production process reveals the dependence of the flow capacity of the sample on time scales.

4.3.3. Cumulative gas production

The 3D simulations allow us to investigate the cumulative gas production. The simulation gives the gas density and pressure at each voxel of the image during gas production. Therefore, we can compute how much gas is produced from the entire domain, as well as, from each of the four material constituents (macro-pores, organic matter, clay, and granular minerals). We compute the theoretical total gas production of the sample as if the gas pressure drops from p_{f_1} to p_{f_2} at every voxel in the image (considering desorption), and use this theoretical total production to normalize the cumulative production rates. Fig. 8 shows the results from the full model, where we plot the cumulative production from the entire sample and the loss of gas from each of the four material constituents. The results for all of the four models are presented in Figs. 9 and 10.

Analysis of the results in Fig. 8 leads to two observations. First, the overall gas production is slightly less than unity, which means that there is gas in the domain that cannot be produced from the right boundary. This 'trapped' gas may stay in macro-pores, organic matter, or clay regions, isolated by the impermeable granular minerals not accessible from the right boundary. In fact, the second largest macro-pores cluster shown in Fig. 3 is isolated by granular minerals, and the gas cannot be produced. Second, production from organic matter contributes the most at low pressure ($p_f = 1$ MPa), while production from the macro-pores dominates at high pressure ($p_f = 50$ MPa). This is because the density contrast between the free-gas and the adsorbed gas is large at low pressure ($\rho_{\mathrm{ad}} = 400\,\mathrm{kg/m^3}$ and $\rho_f = 4.84\,\mathrm{kg/m^3}$ at $p_f = 1$ MPa), where production from desorbed gas can be significant. The contribution from desorption is less at high pressure as the density contrast is much smaller ($\rho_{\mathrm{ad}} = 400\,\mathrm{kg/m^3}$ and $\rho_f = 214.74\,\mathrm{kg/m^3}$ at $p_f = 50$ MPa).

Among the four models, DSA, NDSA, and the full model have the same total production for both low and high pressures. The total production from the DS model is less for low pressure, but more for high pressure (see Figs. 9 and 10). This is because the excess adsorption changes from monotonically increasing at $p_f = 1$ MPa to monotonically decreasing at $p_f = 50$ MPa, as shown in Fig. 11. Therefore, compared to the case with no adsorption/desorption (i.e., the DS model), adsorp-

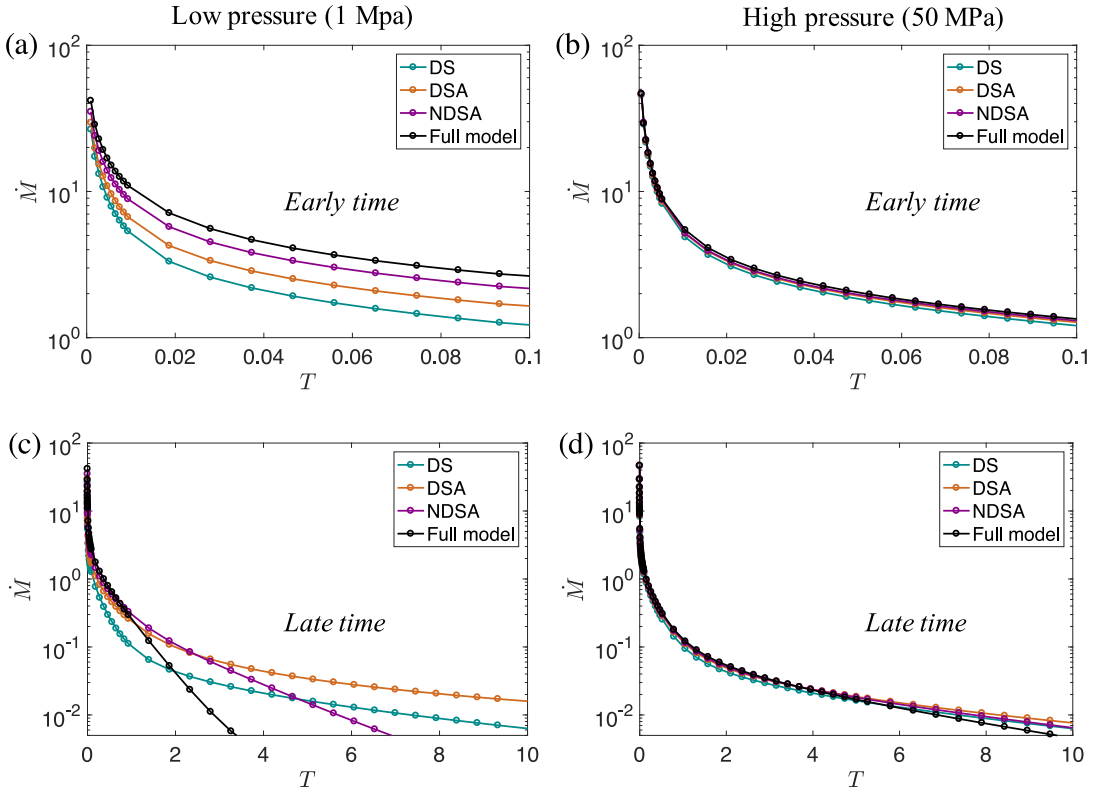

Fig. 7. Simulation of gas production decline on the 3D image using the four models (DS, DSA, NDSA, and full model). (a) and (c) are early and late time decline for a low gas pressure ($p_f = 1$ MPa), and (b) and (d) are early and late time decline for a high gas pressure ($p_f = 50$ MPa).(For interpretation of the references to color in this figure, the reader is referred to the web version of this article.)

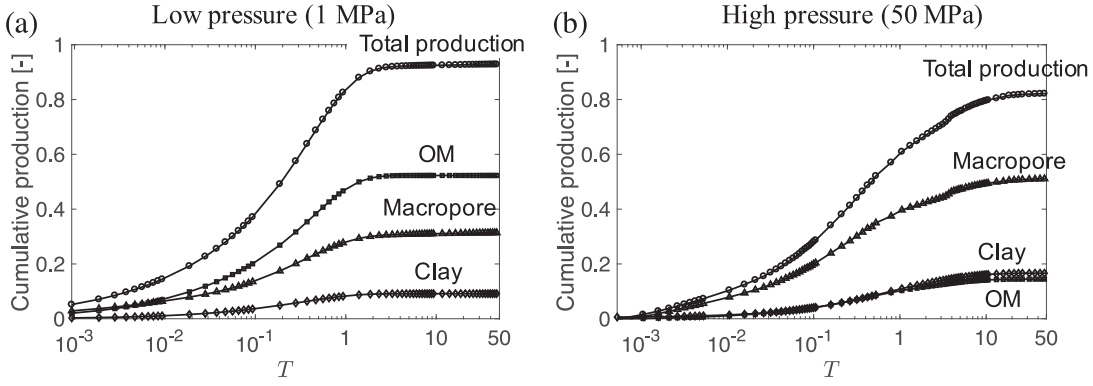

Fig. 8. Simulation of cumulative gas production using the full model. (a) is for low pressure ($p_f = 1$ MPa), and (b) is for high pressure ($p_f = 50$ MPa). Total production as well as mass loss of gas in macro-pores, organic matter, and clay are shown.

tion/desorption leads to more production at low pressure, while less production at high pressure. At low pressure (Fig. 9), we observe that as additional physical mechanisms are included, gas production is accelerated. Production from organic matter has the largest acceleration. However, acceleration of gas production becomes negligible at high pressure as indicated in Fig. 10, where cumulative production curves from the four models are almost identical. This confirms that the non-Darcy effects and surface diffusion become negligible for high gas pressures.

The 3D simulations also allow us to visualize the gas production process at different simulation times. In Fig. 12, we take the low pressure case $p_f = 1$ MPa from the full model as an example to visualize gas production in 3D. We present the evolution of remaining producible gas over dimensionless time ($T = 0, 0.01, 0.1, 1, 50$) during production. The producible gas is defined as the amount of gas that should be produced at each image voxel if gas pressure drops from p_{f_1} to p_{f_2}. At $T = 0$, the macro-pores have the highest producible gas density (mass of producible gas per voxel) indicated by the red color. The green color represents the producible gas density in the organic matter, while light blue indicates the producible gas in clay. The 3D visualization confirms our observations in Fig. 7 that gas production is limited by the macro-pore network before $T = 0.1$, while the nano-porous organic matter and clay become dominant in late time after $T = 1$. Also, from $T = 0$ to $T = 50$, we can see that there is gas in domain (e.g., the red region at $T = 50$) that is not accessible from the right boundary and cannot be produced.

5. Discussions

The simulation results from the micro-continuum model consider both the steady-state apparent permeability and the transient gas production process. The apparent permeability for shale has been a focus

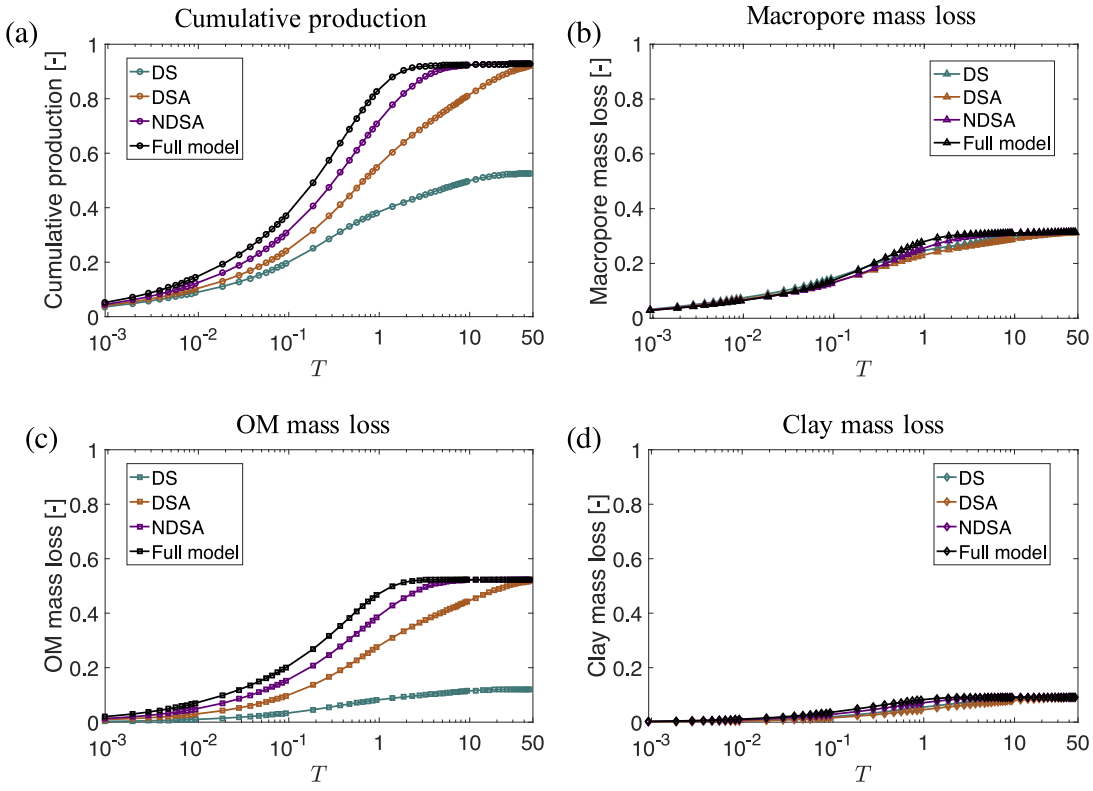

Fig. 9. Simulation of cumulative gas production at low pressure ($p_f = 1$ MPa) using the four models (DS, DSA, NDSA, and full model). (a) shows the total gas production, and (b)–(d) represent the mass loss in the sample from macro-pores, organic matter, and clay, over time. (For interpretation of the references to color in this figure legend, the reader is referred to the web version of this article.)

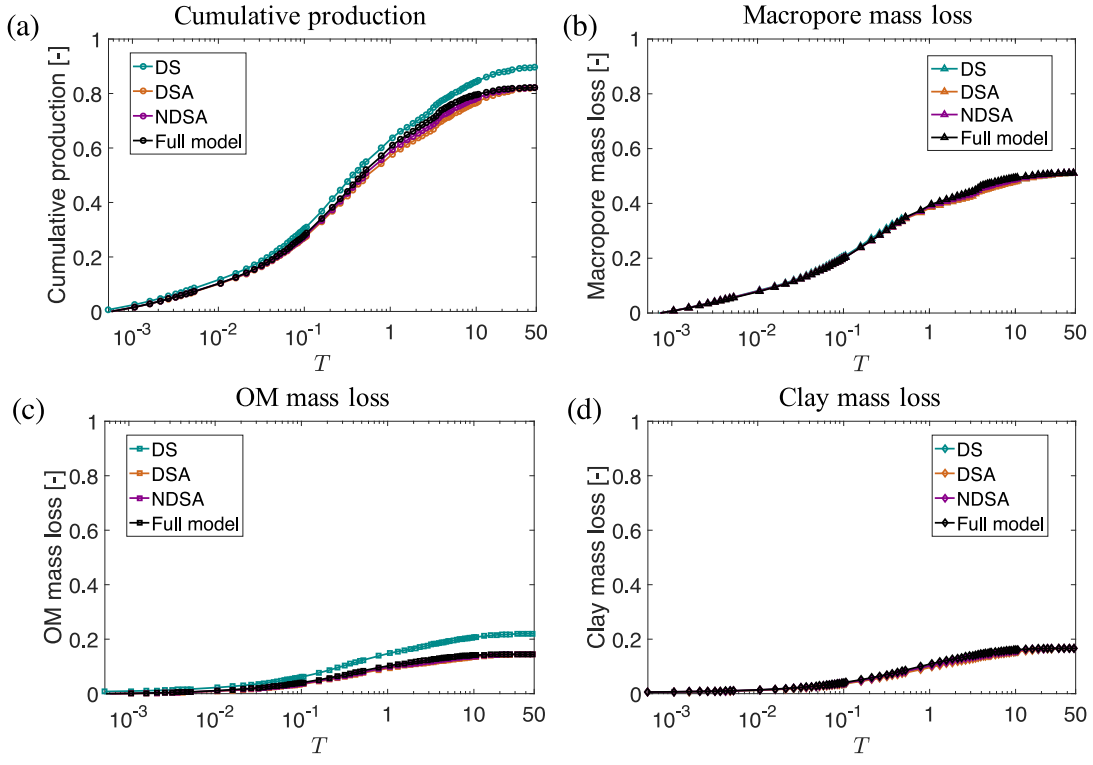

Fig. 10. Simulation of cumulative gas production at high pressure ($p_f = 50$ MPa) using the four models (DS, DSA, NDSA, and full model). (a) shows the total gas production, and (b)–(d) represent the mass loss in the sample from macro-pores, organic matter, and clay, over time. (For interpretation of the references to color in this figure legend, the reader is referred to the web version of this article.)

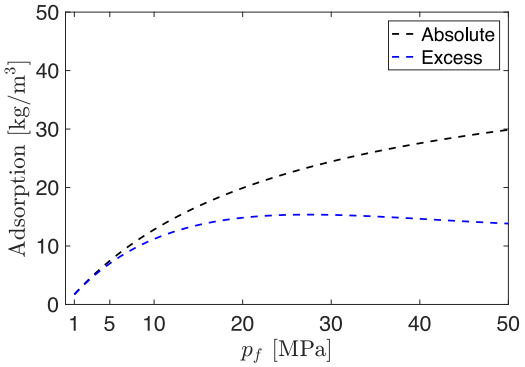

Fig. 11. Absolute (black dashed line) and excess (blue dashed line) adsorbed mass per cubic meter of organic matter as a function of gas pressure for methane using typical parameters for isolated organic matter from organic-rich shale (Rexer et al., 2014).(For interpretation of the references to color in this figure legend, the reader is referred to the web version of this article.)

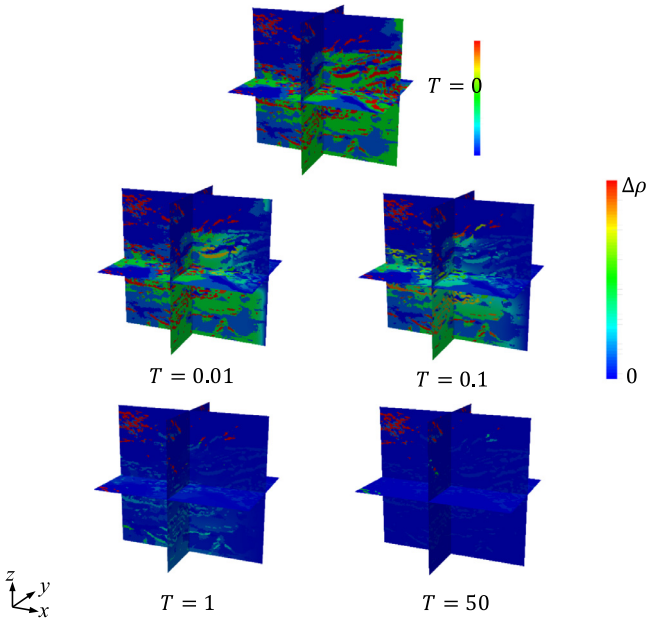

Fig. 12. 3D visualization of gas production at $T = 0, 0.01, 0.1, 1, 50$ for low pressure ($p = 1$ MPa) using the full model. The color represents the remaining producible gas per voxel due to pressure change at the right boundary. Note that the producible gas in organic matter includes both free gas and adsorbed gas.(For interpretation of the references to color in this figure, the reader is referred to the web version of this article.)

of many recent experimental and modeling work. Pressure pulse-decay method, a technique designed to measure permeability of tight rocks (Brace et al., 1968; Dicker and Smits, 1988; Jones, 1997), has been used to measure the apparent permeability of shale core plugs (e.g., Cui et al., 2009; Heller et al., 2014; Abdelmalek et al., 2017). This is done by fitting a 1D model (similar to the 1D model in Section 4.3.1 when non-Darcy effects, adsorption/desorption, and surface diffusion are not included) to the pressure curve from the dynamically changing flow due to the pressure pulse. The pressure pulse-decay method works well for tight rocks, but whether it can be directly applied to the much more complex organic-rich shale is still an open question (Cui et al., 2009; Alnoaimi et al., 2016). Various models have been developed to understand how the transport mechanisms (non-Darcy effects, adsorption/desorption, surface diffusion) control the apparent permeability of shale. For example, bundle-of-tubes models (e.g., Civan, 2010; Darabi et al., 2012)), PNM (e.g., Mehmani et al., 2013; Song et al., 2017), and LBM (e.g., Wang et al., 2017). These models either consider idealized or approximated pore structures (bundle-of-tubes model and PNM models) or only consider the resolved pores and neglect the sub-resolution nano-pore structures (LBM simulations). Our micro-continuum model offers a direct reference solution of gas transport in 3D real digital images of shale that considers both the resolved macro-pores and sub-resolution pore structures. Demonstrated by the two numerical experiments, the micro-continuum model can be used to compute the steady-state apparent permeability as well as analyze the transient behavior of gas transport using a pressure decay setup. The direct reference solutions of gas transport in 3D shale images may provide new insights into the interpretation of pressure pulse-decay experiments shown by the transient analysis in the second numerical experiment.

The micro-continuum modeling framework is able to model gas transport on a high-resolution 3D digital shale image including non-Darcy effects, adsorption/desorption, which offers a quantitative tool to analyze the transport properties of shale. Nevertheless, there are a few challenges that need to be addressed to improve the modeling framework. For example, higher resolution images that can resolve the pores in the sub-resolution nano-porous regions can be helpful to better estimate the intrinsic and apparent permeabilities of the organic matter and clay. When the Stokes flow in macro-pores falls into the slip flow regime, appropriate velocity slip conditions at the wall needs to be developed. The current model has non-zero velocities at the boundaries between macro-pores and the nano-porous regions (organic matter and clay), but the boundaries between macro-pores and the granular minerals are considered as no-slip. Finally, the current computational algorithm based on the Darcy–Brinkman–Stokes framework turns out to be very computationally expensive, which forces us to use a subset of the original full image to reduce the computational cost. Even for the sub-image, it takes a few days to a week to finish one simulation using about 100 processors on a computer cluster. It is therefore desirable to speed up the micro-continuum model, e.g., by developing multiscale algorithms, which is part of our ongoing research.

6. Conclusion

We have developed a micro-continuum pore-scale modeling framework for gas transport in organic-rich shale using high-resolution 3D digital images. We model flow in the resolved macro-pores using the Stokes equation; we consider the sub-resolution nano-porous region (organic matter or clay) as a continuum, and develop an apparent permeability model to include the non-Darcy effects (e.g., slip flow and Knudsen diffusion). Adsorption/desorption and surface diffusion are included in the sub-resolution organic matter region. This modeling framework allows us to investigate the complex transport mechanisms involved in organic-rich shale formations. We apply the micro-continuum model to simulate a 3D FIB-SEM image using two different settings. The first setting allows for computing an apparent permeability, and the other setting simulates the transient gas production process. Our simulation results show that non-Darcy and surface diffusion effects are important at low gas pressure (1 MPa); these mechanisms become negligible at high pressure (50 MPa). Our gas production analysis indicates that a simple pressure dependent apparent permeability may not represent the transport properties of organic-rich shale. Depending on the pore structures of the shale image, different time scales may need to be introduced to better describe the transport properties of shale at a fixed gas pressure.

Acknowledgment

The image datasets were provided by L. Ma, P. D. Lee and K. Taylor and generated through funding from NERC-UK (NE/M001458/1), the Research Complex at Harwell, and the European Union Horizon 2020 716 Research and Innovation Program under the ShaleXenvironmenT project, (grant no. 640979). We thank C. Soulaine for discussions on OpenFOAM and Y. Mehmani for discussions on image processing. This

work is supported in part by TOTAL through the Stanford TOTAL enhanced modeling of source rock (STEMS) project.

Appendix A. Equation-of-state and viscosity equation for methane

We use the empirical correlation from Mahmoud (2014) as the equation of state for methane, and follow the empirical equation from Lee et al. (1966) to compute viscosity. The empirical correlation from Mahmoud (2014) is derived using the compressibility factor approach. Here, we outline the empirical equations for density and viscosity respectively.

We rescale the pressure and temperature by the critical pressure and temperature and define the dimensionless reduced pressure and temperature

$$p_{f,r} = \frac{p_f}{p_{f,\text{critical}}}, \tag{A.1}$$

$$T_r = \frac{T}{T_{\text{critical}}}, \tag{A.2}$$

where p_f and T are the absolute pressure and temperature of free methane; $p_{f,\text{crtical}}$ and T_{critical} are the critical pressure and temperature. Then, the empirical correlation for the compressibility factor, Z, has the following form

$$Z = 0.702e^{-2.5T_{f,r}}p_{f,r}^2 - 5.524e^{-2.5T_{f,r}}p_{f,r} + 0.044T_{f,r}^2 - 0.164T_{f,r} + 1.15. \tag{A.3}$$

Substituting Z to Eq. (1) gives the density of methane. After we obtain density, we can compute viscosity using the equations from Lee et al. (1966).

$$\mu_f = 10^{-7}Se^{X(0.001\rho_f)^Y}, \tag{A.4}$$

where

$$S = \frac{(9.379 + 0.0160M)(1.8T)^{1.5}}{209.2 + 19.26M + 1.8T}, \tag{A.5}$$

$$X = 3.448 + \frac{986.4}{1.8T} + 0.01009M, \tag{A.6}$$

$$Y = 2.4 - 0.2X. \tag{A.7}$$

μ_f, ρ_f, M, T in Eqs. (A.4), (A.5) and (A.6) all have SI base units. Note: (1) some of the coefficient constants in Eqs. (A.4), (A.5) and (A.6) are modified from Lee et al. (1966) based on Eq. (62) in Mahmoud (2014); (2) the temperature in Lee et al. (1966) is in Rankine scale (°R) and we converted it to Kelvin scale (K) by multiplying by 1.8. We have compared the density and viscosity of free methane with the methane density and viscosity from the NIST fluid database (Lemmon et al., 1998), and we observe a maximum relative error less than 5%.

Appendix B. Scaling arguments for Eq. (15)

Here we present a scaling argument to show that the momentum equation for compressible flow can be simplified to the form of Eq. (15). We define the following dimensionless variables and groups

$$\widetilde{\mathbf{x}} = \frac{\mathbf{x}}{l_c}, \widetilde{t} = \frac{t}{t_c}, \widetilde{\mathbf{u}}_f = \frac{\mathbf{u}_f}{l_c/t_c}, \widetilde{p}_f = \frac{p_f}{\mu_c u_c/l_c}, \widetilde{\mathbf{g}} = \frac{\mathbf{g}}{g}, \widetilde{\rho}_f = \frac{\rho_f}{\rho_{f,c}}, \widetilde{\mu}_f = \frac{\mu_f}{\mu_{f,c}}, \tag{B.1}$$

$$\text{Re} = \frac{\rho_{f,c}u_{f,c}l_c}{\mu_{f,c}}, \text{Fr} = \frac{gl_c}{u_{f,c}^2}, \tag{B.2}$$

where $u_{f,c}$, $p_{f,c}$ are characteristic velocity and pressure; l_c and t_c are characteristic length and time scales; $\mu_{f,c}$ and $\rho_{f,c}$ are characteristic viscosity and density; Re is the Reynolds number and Fr is the Froude number that defines the relative importance of gravity and viscosity effects.

Substituting the nondimensionalized variables to Eq. (15) with the time derivative term, we obtain

$$\text{Re}\frac{\partial(\widetilde{\rho}_f\widetilde{\mathbf{u}}_f)}{\partial\widetilde{t}} = -\nabla\widetilde{p}_f + \frac{\text{Re}}{\text{Fr}}\widetilde{\rho}_f\widetilde{\mathbf{g}} + \nabla\cdot\left(\widetilde{\mu}_f\nabla\widetilde{\mathbf{u}}_f\right) + \frac{1}{3}\nabla\left(\widetilde{\mu}_f\nabla\cdot\widetilde{\mathbf{u}}_f\right). \tag{B.3}$$

For the extremely tight shale rock with nanometer-scale pore structures, the Reynolds number $\text{Re} \ll 1$, which means that the time derivative term is eligible compared to the terms related to the pressure gradient and the viscous forces.

Appendix C. Numerical algorithm for the micro-continuum model

We introduce the numerical algorithm to solve Eqs. (16) and (17) based on the PIMPLE algorithm in OpenFOAM. Discretization of the equations here follows in part chapter 3 of Jasak (1996), which presents discretizations of the Navier–Stokes equations for incompressible flow.

Discretization

The PIMPLE algorithm solves velocity and pressure implicitly through sequentially coupling. Here, we derive the discretized forms of the momentum and pressure equations.

Discretizing the integral form of the momentum Eq. (17) over a control volume V with backward Euler time stepping gives

$$a_P^{n+1}\mathbf{u}_P^{n+1} = \sum_{NP} a_{NP}^{n+1}\mathbf{u}_{NP}^{n+1} - \nabla p^{n+1} + \rho_f^{n+1}\mathbf{g}, \tag{C.1}$$

where both sides of the equation are divided by the control volume V. $\mathbf{u}_P$ is the cell-centered velocity of the current cell, and $\mathbf{u}_{NP}$ denotes the cell-centered velocity of the neighbouring cells; subscripts '$_P$' and '$_{NP}$' denote the current cell and neighbouring cells, respectively. a_P^{n+1} consists coefficients contributed by the divergence term $(\nabla\cdot\left(\frac{\mu_f}{\phi}\nabla\mathbf{u}_f\right))$ and the apparent Darcy term $\mu_f k_a^{-1}\mathbf{u}_f$, while a_{NP}^{n+1} only has coefficients from the divergence term. The superscript 'n' and 'n + 1' denote time steps. We note that the pressure gradient term and the gravity term are not discretized in space at this stage.

Now we formulate the pressure equation based on the semi-discretized form of the momentum Eq. (C.1). We divide both sizes of Eq. (C.1) by a_P and interpolate the equation at the cell face, and obtain

$$\left(\mathbf{u}_P^{n+1}\right)_{\text{face}} = \left(\frac{1}{a_P^{n+1}}\right)_{\text{face}}\left(\sum_{NP} a_{NP}^{n+1}\mathbf{u}_{NP}^{n+1}\right)_{\text{face}} - \left(\frac{1}{a_P^{n+1}}\right)_{\text{face}}\left(\nabla p^{n+1}\right)_{\text{face}} + \left(\frac{1}{a_P^{n+1}}\right)_{\text{face}}\left(\rho_f^{n+1}\mathbf{g}\right)_{\text{face}}. \tag{C.2}$$

Substituting Eq. (C.2) into the integral form of the mass balance Eq. (16), we obtain the pressure equation

$$A_1^{n+1}\frac{{p_f}^{n+1} - {p_f}^{n}}{\Delta t} - \sum_{\text{face}} S\cdot\left[A_2^{n+1}\left(\nabla {p_f}^{n+1}\right)_{\text{face}}\right] + \sum_{\text{face}} S \cdot\left[A_3^{n+1}\left(\sum_{NP} a_{NP}^{n+1}\mathbf{u}_{NP}^{n+1}\right)_{\text{face}}\right] + \sum_{\text{face}} S\cdot\left[A_3^{n+1}\left(\rho_f^{n+1}\mathbf{g}\right)_{\text{face}}\right] = 0, \tag{C.3}$$

where S is the area of the cell face, $A_1 = \phi\frac{\partial\rho_f}{\partial p_f} + \delta_{\text{om}}[(1-\frac{\rho_f}{\rho_{\text{ad}}})n_{\text{ad}}^{\max}\frac{K}{(1+Kp_f)^2} - \frac{n_{\text{ad}}^{\max}Kp_f}{\rho_{\text{ad}}(1+Kp_f)}\frac{\partial\rho_f}{\partial p_f}]$, $A_2 = (\rho_f)_{\text{face}}(\frac{1}{a_P})_{\text{face}} + (\delta_{\text{om}}D_s n_{\text{ad}}^{\max}\frac{K}{(1+Kp_f)^2})_{\text{face}}$, $A_3 = \left(\rho_f\right)_{\text{face}}\left(\frac{1}{a_P}\right)_{\text{face}}$.

Now we need to solve the discretized momentum Eq. (C.1) and pressure Eq. (C.3).

Solution procedure

We introduce the solution procedure to solve the discrete momentum and pressure Eqs. (C.1) and (C.3) following the PIMPLE algorithm. The momentum and pressure equations are solved sequentially in PIMPLE,

and iterations are required between the velocity and pressure solutions within one time step to reach convergence before moving on to the next time step. The momentum–pressure iterations are similar to the SIMPLE algorithm, and are referred to as outer correction loops. Within each momentum–pressure correction loop, pressure can be solved multiple times followed by explicit velocity corrections after the implicit solution of the momentum equation. The pressure and velocity corrections within a momentum–pressure correction loop are referred to as inner corrections, which is similar to the PISO algorithm. Here we outline the solution procedure from time step n to time step n + 1, and from outer correction loop i to i + 1. The inner corrections are described in words.

1. Solve momentum Eq. (C.1). This step is called momentum predictor. The pressure gradient is computed using pressure distribution from the outer correction loop *i*, and the velocity is under-relaxed in an implicit manner as the following

$$a_P^{n+1,i}\mathbf{u}_P^{n+1,i+1,*}+\frac{1-\alpha_u}{\alpha_u}\mathbf{u}_P^{n+1,i+1,*}=\sum_{NP}a_{NP}^{n+1,i}\mathbf{u}_{NP}^{n+1,i+1,*}-\nabla {p_f}^{n+1,i}+\rho_f\mathbf{g}+\frac{1-\alpha_u}{\alpha_u}a_P^{n+1,i}\mathbf{u}_P^{n+1,i}, \tag{C.4}$$

where α_u is the under-relaxation factor for velocity. We denote the updated velocity with a superscript "*" because it is an approximation with the pressure field from the previous outer correction loop.
2. Solve pressure Eq. (C.3) with updated velocity $\mathbf{u}^{n+1,i+1,*}$ from step 1. Then update velocity in an explicit manner following Eq. (C.2) using the new pressure, and solve pressure Eq. (C.3) again. This is called inner correction. We repeat the inner correction until we reach the specified number of inner corrections.
3. Under relax the pressure solution based on Eq. (C.5)

$${p_f}^{n+1,i+1}={p_f}^{n+1,i}+\alpha_p\left({p_f}^{n+1,i+1,*}-{p_f}^{n+1,i}\right), \tag{C.5}$$

where ${p_f}^{n+1,i}$ is the pressure from the previous outer correction loop *i*, ${p_f}^{n+1,i+1,*}$ is the pressure obtained after step 2, ${p_f}^{n+1,i+1}$ is the pressure that will be used in the next momentum predictor to start the next outer correction loop, and α_p is the under-relaxation factor for pressure.
4. Repeat steps 1–3 for the next outer correction loop until reaching a specified number of outer correction loops or specified residual tolerance for velocity and pressure.
5. Repeat steps 1–4 for the next time step until reaching the end of the simulation time.

Appendix D. Derivations of the 1D model in Section 4.3.1

Here we present the details to derive Eq. (23) from Eq. (22). The first term of Eq. (22)

$$\frac{\partial\left(\bar{\phi}\rho_f\right)}{\partial t}=\bar{\phi}\frac{\partial\rho_f}{\partial t}=\bar{\phi}\frac{\partial\rho_f}{\partial p_f}\frac{\partial p_f}{\partial t}. \tag{D.1}$$

The second term of Eq. (22)

$$\bar{\gamma}_{\mathrm{om}}\frac{\partial}{\partial t}\left[\left(1-\frac{\rho_f}{\rho_{\mathrm{ad}}}\right)n_{\mathrm{ad}}\right]=\bar{\gamma}_{\mathrm{om}}n_{\mathrm{ad}}^{\max}\frac{K}{\left(1+Kp_f\right)^2}\left(1-\frac{\rho_f}{\rho_{\mathrm{ad}}}\right)\frac{\partial p_f}{\partial t}-\bar{\gamma}_{\mathrm{om}}\frac{n_{\mathrm{ad}}^{\max}Kp_f}{\rho_{\mathrm{ad}}\left(1+Kp_f\right)}\frac{\partial\rho_f}{\partial p_f}\frac{\partial p_f}{\partial t}. \tag{D.2}$$

The third term of Eq. (22)

$$\begin{aligned}\frac{\partial\left(\rho_f u_{f,x}+\bar{\gamma}_{\mathrm{om}}\rho_{\mathrm{ad}}u_{\mathrm{ad},x}\right)}{\partial x}&=\frac{\partial\left(\rho_f u_{f,x}\right)}{\partial x}+\frac{\partial\left(\bar{\gamma}_{\mathrm{om}}\rho_{\mathrm{ad}}u_{\mathrm{ad},x}\right)}{\partial x}=-\rho_f\frac{\bar{k}_a}{\mu_f}\frac{\partial^2p_f}{\partial x^2}\\&\quad-\bar{\gamma}_{\mathrm{om}}\rho_{\mathrm{ad}}D_sn_{\mathrm{ad}}^{\max}\frac{\partial}{\partial x}\left[\frac{K}{\left(1+Kp_f\right)^2}\frac{\partial p_f}{\partial x}\right]\\&=-\rho_f\frac{\bar{k}_a}{\mu_f}\frac{\partial^2p_f}{\partial x^2}\\&\quad-\bar{\gamma}_{\mathrm{om}}\rho_{\mathrm{ad}}D_sn_{\mathrm{ad}}^{\max}\frac{K}{\left(1+Kp_f\right)^2}\frac{\partial^2p_f}{\partial x^2}\\&\quad-\bar{\gamma}_{\mathrm{om}}\rho_{\mathrm{ad}}D_sn_{\mathrm{ad}}^{\max}\frac{2K^2}{\left(1+Kp_f\right)^3}\left(\frac{\partial p_f}{\partial x}\right)^2.\end{aligned} \tag{D.3}$$

Now we show that $\frac{2K^2}{\left(1+Kp_f\right)^3}\left(\frac{\partial p_f}{\partial x}\right)^2\ll\frac{K}{\left(1+Kp_f\right)^2}\frac{\partial^2p_f}{\partial x^2}$. These two terms have the following scaling

$$\frac{2K^2}{\left(1+Kp_f\right)^3}\left(\frac{\partial p_f}{\partial x}\right)^2\sim\frac{2K^2}{\left(1+Kp_f\right)^3}\left(\frac{\Delta p}{L_x}\right)^2, \tag{D.4}$$

$$\frac{K}{\left(1+Kp_f\right)^2}\frac{\partial^2p_f}{\partial x^2}\sim\frac{K}{\left(1+Kp_f\right)^2}\frac{\Delta p}{L_x^2}. \tag{D.5}$$

We take a ratio of the two terms, and obtain $\left[\frac{2K^2}{\left(1+Kp_f\right)^3}\left(\frac{\Delta p}{L_x}\right)^2\right]/\left[\frac{K}{\left(1+Kp_f\right)^2}\frac{\Delta p}{L_x^2}\right]=\frac{2K\Delta p}{1+Kp_f}<2K\Delta p=8\times10^{-6}\ll1$. Therefore, $\frac{2K^2}{\left(1+Kp_f\right)^3}\left(\frac{\partial p_f}{\partial x}\right)^2$ can be neglected, so the third term of Eq. (22) can be approximated as

$$\frac{\partial\left(\rho_f u_{f,x}+\bar{\gamma}_{\mathrm{om}}\rho_{\mathrm{ad}}u_{\mathrm{ad},x}\right)}{\partial x}\approx-\rho_f\frac{\bar{k}_a}{\mu_f}\frac{\partial^2p_f}{\partial x^2}-\bar{\gamma}_{\mathrm{om}}\rho_{\mathrm{ad}}D_sn_{\mathrm{ad}}^{\max}\frac{K}{\left(1+Kp_f\right)^2}\frac{\partial^2p_f}{\partial x^2}. \tag{D.6}$$

Putting together all three terms of Eq. (22), we get

$$\left(\bar{\phi}\frac{\partial\rho_f}{\partial p_f}+\bar{\gamma}_{\mathrm{om}}n_{\mathrm{ad}}^{\max}\frac{K}{\left(1+Kp_f\right)^2}\left(1-\frac{\rho_f}{\rho_{\mathrm{ad}}}\right)-\bar{\gamma}_{\mathrm{om}}\frac{n_{\mathrm{ad}}^{\max}Kp_f}{\rho_{\mathrm{ad}}\left(1+Kp_f\right)}\frac{\partial\rho_f}{\partial p_f}\right)\frac{\partial p_f}{\partial t}=\left(\rho_f\frac{\bar{k}_a}{\mu_f}+\bar{\gamma}_{\mathrm{om}}\rho_{\mathrm{ad}}D_sn_{\mathrm{ad}}^{\max}\frac{K}{\left(1+Kp_f\right)^2}\right)\frac{\partial^2p_f}{\partial x^2}. \tag{D.7}$$

Rearranging Eq. (D.7) gives the Eq. (23).

References

Abdelmalek, B., Karpyn, Z., Liu, S., Yoon, H., Dewers, T., 2018. Gas permeability measurements from pressure pulse decay laboratory data using pseudo-pressure and pseudo–time transformations. J. Pet. Explor. Prod. Technol. 8, 839–847.

Akkutlu, I.Y., Efendiev, Y., Savatorova, V., 2015. Multi-scale asymptotic analysis of gas transport in shale matrix. Transp. Porous Media 107 (1), 235–260.

Alnoaimi, K.R., Duchateau, C., Kovscek, A.R., 2016. Characterization and measurement of multiscale gas transport in shale-core samples. SPE J. 21 (02), 573–588.

Bakhshian, S., Shi, Z., Sahimi, M., Tsotsis, T.T., Jessen, K., 2018. Image-based modeling of gas adsorption and deformation in porous media. Sci. Rep. 8 (1), 8249.

Beavers, G.S., Joseph, D.D., 1967. Boundary conditions at a naturally permeable wall. J. Fluid Mech. 30 (1), 197–207.

Beskok, A., Karniadakis, G.E., 1999. Report: a model for flows in channels, pipes, and ducts at micro and nano scales. Microscale Thermophys. Eng. 3 (1), 43–77.

Blunt, M.J., 2017. Multiphase Flow in Permeable Media: a Pore-Scale Perspective. Cambridge University Press.

Blunt, M.J., Bijeljic, B., Dong, H., Gharbi, O., Iglauer, S., Mostaghimi, P., Paluszny, A., Pentland, C., 2013. Pore-scale imaging and modelling. Adv. Water Resour. 51, 197–216.

Brace, W., Walsh, J., Frangos, W., 1968. Permeability of granite under high pressure. J. Geophys. Res. 73 (6), 2225–2236.

Brinkman, H., 1949. A calculation of the viscous force exerted by a flowing fluid on a dense swarm of particles. Appl. Sci. Res. 1 (1), 27–34.

Bultreys, T., Van Hoorebeke, L., Cnudde, V., 2015. Multi-scale, micro-computed tomography-based pore network models to simulate drainage in heterogeneous rocks. Adv. Water Resour. 78, 36–49.

Chalmers, G.R., Bustin, R.M., Power, I.M., 2012. Characterization of gas shale pore systems by porosimetry, pycnometry, surface area, and field emission scanning electron microscopy/transmission electron microscopy image analyses: examples from the Barnett, Woodford, Haynesville, Marcellus, and Doig units. AAPG Bull. 96 (6), 1099–1119.

Chen, L., Zhang, L., Kang, Q., Viswanathan, H.S., Yao, J., Tao, W., 2015. Nanoscale simulation of shale transport properties using the lattice Boltzmann method: permeability and diffusivity. Sci. Rep. 5, 8089.

Civan, F., 2010. Effective correlation of apparent gas permeability in tight porous media. Transp. Porous Media 82 (2), 375–384.

Clarkson, C.R., Solano, N., Bustin, R.M., Bustin, A., Chalmers, G., He, L., Melnichenko, Y.B., Radliński, A., Blach, T.P., 2013. Pore structure characterization of North American shale gas reservoirs using USANS/SANS, gas adsorption, and mercury intrusion. Fuel 103, 606–616.
Cui, X., Bustin, A., Bustin, R.M., 2009. Measurements of gas permeability and diffusivity of tight reservoir rocks: different approaches and their applications. Geofluids 9 (3), 208–223.
Curtis, M.E., Sondergeld, C.H., Ambrose, R.J., Rai, C.S., 2012. Microstructural investigation of gas shales in two and three dimensions using nanometer-scale resolution imaging. AAPG Bull. 96 (4), 665–677.
Darabi, H., Ettehad, A., Javadpour, F., Sepehrnoori, K., 2012. Gas flow in ultra-tight shale strata. J. Fluid Mech. 710, 641–658.
Dicker, A., Smits, R., 1988. A practical approach for determining permeability from laboratory pressure-pulse decay measurements. In: Proceedings of the International Meeting on Petroleum Engineering. Society of Petroleum Engineers.
Edwards, R.W., Celia, M.A., Bandilla, K.W., Doster, F., Kanno, C.M., 2015. A model to estimate carbon dioxide injectivity and storage capacity for geological sequestration in shale gas wells. Environ. Sci. Technol. 49 (15), 9222–9229.
EIA, 2017. Natural Gas Annual Report. U.S. Energy Information Administration.
Gensterblum, Y., Ghanizadeh, A., Cuss, R.J., Amann-Hildenbrand, A., Krooss, B.M., Clarkson, C.R., Harrington, J.F., Zoback, M.D., 2015. Gas transport and storage capacity in shale gas reservoirs–a review. Part A: transport processes. J. Unconv. Oil Gas Resour. 12, 87–122.
Goyeau, B., Lhuillier, D., Gobin, D., Velarde, M., 2003. Momentum transport at a fluid—porous interface. Int. J. Heat Mass Transf. 46 (21), 4071–4081.
Heller, R., Vermylen, J., Zoback, M., 2014. Experimental investigation of matrix permeability of gas shales. AAPG Bull. 98 (5), 975–995.
Heller, R., Zoback, M., 2014. Adsorption of methane and carbon dioxide on gas shale and pure mineral samples. J. Unconv. Oil Gas Resour. 8, 14–24.
Issa, R.I., 1986. Solution of the implicitly discretised fluid flow equations by operator-splitting. J. Comput. Phys. 62 (1), 40–65.
Jasak, H., 1996. Error Analysis and Estimation for the Finite Volume Method with Applications to Fluid Flows. University of London Imperial College Ph.D. thesis.
Javadpour, F., 2009. Nanopores and apparent permeability of gas flow in mudrocks (shales and siltstone). J. Can. Pet. Technol. 48 (08), 16–21.
Jones, S., 1997. A technique for faster pulse-decay permeability measurements in tight rocks. SPE Form. Eval. 12 (01), 19–26.
Karniadakis, G.E., Beskok, A., Aluru, N., 2005. Microflows and Nanoflows: Fundamentals and Simulation. Springer.
Kelly, S., El-Sobky, H., Torres-Verdín, C., Balhoff, M.T., 2016. Assessing the utility of FIB-SEM images for shale digital rock physics. Adv. Water Resour. 95, 302–316.
Klinkenberg, L., 1941. The permeability of porous media to liquids and gases. Drilling and Production Practice. American Petroleum Institute.
Landry, C.J., Prodanović, M., Eichhubl, P., 2016. Direct simulation of supercritical gas flow in complex nanoporous media and prediction of apparent permeability. Int. J. Coal Geol. 159, 120–134.
Lee, A.L., Gonzalez, M.H., Eakin, B.E., 1966. The viscosity of natural gases. J. Pet. Technol. 18 (08), 997–1000.
Lemmon, E., McLinden, M., Friend., D., 1998. Thermophysical properties of fluid systems. In: Linstrom, P., Mallard, W. (Eds.), NIST Chemistry WebBook, NIST Standard Reference Database Number 69. National Institute of Standards and Technology, Gaithersburg MD.
Lunati, I., Lee, S., 2014. A dual-tube model for gas dynamics in fractured nanoporous shale formations. J. Fluid Mech. 757, 943–971.
Ma, L., Fauchille, A.-L., Dowey, P.J., Pilz, F.F., Courtois, L., Taylor, K.G., Lee, P.D., 2017. Correlative multi-scale imaging of shales: a review and future perspectives. Geol. Soc. Lond. Spec. Publ. 454 (1), 175–199.
Ma, L., Slater, T., Dowey, P.J., Yue, S., Rutter, E.H., Taylor, K.G., Lee, P.D., 2018. Hierarchical integration of porosity in shales. Sci. Rep. 8 (1), 11683.
Ma, L., Taylor, K.G., Lee, P.D., Dobson, K.J., Dowey, P.J., Courtois, L., 2016. Novel 3D centimetre-to nano-scale quantification of an organic-rich mudstone: the Carboniferous Bowland Shale, Northern England. Mar. Pet. Geol. 72, 193–205.
Mahmoud, M., 2014. Development of a new correlation of gas compressibility factor (Z–factor) for high pressure gas reservoirs. J. Energy Resour. Technol. 136 (1), 012903.
Mason, E.A., Malinauskas, A., 1983. Gas Transport in Porous Media: the Dusty-Gas Model, 17. Elsevier Science Ltd.
Medveď, I., Černỳ, R., 2011. Surface diffusion in porous media: a critical review. Microporous Mesoporous Mater. 142 (2), 405–422.
Mehmani, A., Prodanović, M., 2014. The effect of microporosity on transport properties in porous media. Adv. Water Resour. 63, 104–119.
Mehmani, A., Prodanović, M., Javadpour, F., 2013. Multiscale, multiphysics network modeling of shale matrix gas flows. Transp. Porous Media 99 (2), 377–390.
Patankar, S., 1980. Numerical Heat Transfer and Fluid Flow. CRC press.
Rexer, T.F., Mathia, E.J., Aplin, A.C., Thomas, K.M., 2014. High-pressure methane adsorption and characterization of pores in Posidonia shales and isolated kerogens. Energy Fuels 28 (5), 2886–2901.
Ross, D.J., Bustin, R.M., 2009. The importance of shale composition and pore structure upon gas storage potential of shale gas reservoirs. Mar. Pet. Geol. 26 (6), 916–927.
Rouquerol, J., Avnir, D., Fairbridge, C., Everett, D., Haynes, J., Pernicone, N., Ramsay, J., Sing, K., Unger, K., 1994. Recommendations for the characterization of porous solids (technical report). Pure Appl. Chem. 66 (8), 1739–1758.
Ruthven, D.M., 1984. Principles of Adsorption and Adsorption Processes. John Wiley & Sons.
Sakhaee-Pour, A., Bryant, S., 2012. Gas permeability of shale. SPE Reserv. Eval. Eng. 15 (04), 401–409.
Scheibe, T.D., Perkins, W.A., Richmond, M.C., McKinley, M.I., Romero-Gomez, P.D., Oostrom, M., Wietsma, T.W., Serkowski, J.A., Zachara, J.M., 2015. Pore-scale and multiscale numerical simulation of flow and transport in a laboratory-scale column. Water Resour. Res. 51 (2), 1023–1035.
Sondergeld, C.H., Ambrose, R.J., Rai, C.S., Moncrieff, J., 2010. Micro-structural studies of gas shales. In: Proceedings of the SPE Unconventional Gas Conference. Society of Petroleum Engineers.
Song, W., Yao, J., Ma, J., Couples, G., Li, Y., 2017. Assessing relative contributions of transport mechanisms and real gas properties to gas flow in nanoscale organic pores in shales by pore network modelling. Int. J. Heat Mass Transf. 113, 524–537.
Soulaine, C., Tchelepi, H.A., 2016. Micro-continuum approach for pore-scale simulation of subsurface processes. Transp. Porous Media 113 (3), 431–456.
Wang, J., Chen, L., Kang, Q., Rahman, S.S., 2016. The lattice Boltzmann method for isothermal micro-gaseous flow and its application in shale gas flow: a review. Int. J. Heat Mass Transf. 95, 94–108.
Wang, J., Kang, Q., Chen, L., Rahman, S.S., 2017. Pore-scale lattice Boltzmann simulation of micro-gaseous flow considering surface diffusion effect. Int. J. Coal Geol. 169, 62–73.
Wu, K., Li, X., Guo, C., Wang, C., Chen, Z., 2016. A unified model for gas transfer in nanopores of shale-gas reservoirs: coupling pore diffusion and surface diffusion. SPE J. 21 (05), 1–583.
Wu, T., Li, X., Zhao, J., Zhang, D., 2017. Mutiscale pore structure and its effect on gas transport in organic-rich shale. Water Resour. Res. 53, 5438–5450.
Wu, T., Zhang, D., 2016. Impact of adsorption on gas transport in nanopores. Sci. Rep. 6, 23629.
Xiong, X., Devegowda, D., Villazon, M., German, G., Sigal, R.F., Civan, F., 2012. A fully–coupled free and adsorptive phase transport model for shale gas reservoirs including non-darcy flow effects. In: Proceedings of the SPE Annual Technical Conference and Exhibition. Society of Petroleum Engineers.
Zhang, T., Ellis, G.S., Ruppel, S.C., Milliken, K., Yang, R., 2012. Effect of organic-matter type and thermal maturity on methane adsorption in shale-gas systems. Org. Geochem. 47, 120–131.